NEUROTRANSMITTER MEASUREMENTS IN THE HUMAN BRAIN AT 3 TESLA AND 7 TESLA

By

Subechhya Pradhan

Dissertation

Submitted to the Faculty of the

Graduate School of Vanderbilt University

in partial fulfillment of the requirements

for the degree of

DOCTOR OF PHILOSOPHY

in

Physics

May, 2013

Nashville, Tennessee

Approved:

Professor John C. Gore

Professor David Ernst

Professor Malcolm J. Avison

Professor Thomas Yankeelov

Professor Daniel Gochberg

© Copyright by Subechhya Pradhan 2013

All Rights Reserved

To *dadu*, *mamu* and *bhai*

who gave up their own dreams so I could realize mine

and

To *dada* and *nanu*

for their unconditional love

ACKNOWLEDGEMENTS

My gratitude to my adviser and mentor John Gore for his unwavering support and guidance throughout this process. From him I learned to see the forest for the trees.

I am grateful to Kevin Waddell for teaching me MR spectroscopy and many life skills.

Many thanks to Jim Joers who was my rudder at critical junctures.

Jay Moore, Sepideh Shokouhi and Jeff Hammonds – It was a blessing to have your friendship.

I am grateful to the Nashville Nepali community for a vibrant social life.

I am thankful to *sanu* for being my cheerleader through all the highs and the lows. You are the sunshine of my life.

TABLE OF CONTENTS

DEDICATION iii

ACKNOWLEDGEMENTS iv

LIST OF TABLES viii

LIST OF FIGURES ix

LIST OF ABBREVIATIONS xii

I. INTRODUCTION 1
- 1.1 Nuclear magnetism 1
- 1.2 Effect of radio frequency (RF) field on the spin in magnetic field 4
- 1.3 Relaxation processes 5
- 1.4 Localization 6
- 1.5 Pulse sequences 7
  - PRESS 7
  - MEGA-PRESS 8
- 1.6 Practical considerations 11
  - Signal-to-noise 11
  - Baseline 12
  - B_0 inhomogeniety 13
  - B_1 inhomogeniety 13

II. SIMULATION AND QUANTIFICATION OF NEUROTRANSMITTER MEASUREMENTS BY MRS 15

- 2.1 Simulated basis set 15
- 2.2 Density Matrix Simulations 16
- 2.3 Normalizing the simulated spectrum 18
- 2.4 Quantification 20
- 2.5 LCModel 20
  - 2.5.1 Making basis set for LCModel 22
- 2.6 Interpreting LCModel Results 24
- 2.7 Cramer-Rao Lower Bounds 26

III. OPTIMIZATION OF DETECTION PARAMETERS FOR METABOLITES AT 7 TESLA 27
- 3.2 Methods 29
  - 3.2.1 Spectral Simulation 29
  - 3.2.2 Statistics 30
  - 3.2.3 *In vivo* experiments. 31
- 3.3 Results and Discussion 32

3.3.1 CRLB trends with echo-time 33
3.3.2 CRLB vary with molecular structure 34
3.3.3 CRLB dependence on linewidth. 37
3.3.4 Strategies for simultaneous detection of inositol compounds and amino acids. 38
3.3.5 CRLBs with TE-averaging schemes 40
3.3.6 Basis set composition 42
3.4 Conclusions 43

IV. IMPLEMENTATION AND COMPARISON OF GABA MEASUREMENTS AT 3 TESLA AND 7 TESLA 46

4.1 Introduction 46
4.2 Methods 48
4.2.1 Imaging: 48
4.2.2 Spectroscopy 48
4.2.3 Post-processing 51
4.2.4 Analysis 51
4.2.5 Chemical shift displacement calculations 52
4.3 Results and discussion 53
4.3.1 3T vs. 7T measurement 53
4.3.2 Effect of RF and bandwidth at 7 Tesla 56
4.3.3 Chemical shift displacement errors 57
4.4 Conclusions 59

V TIME-RESOLVED MRS 60

5.1 Introduction 60
5.2 Method 62
5.2.1 Imaging 62
5.2.2 Spectroscopy 63
5.2.3 Data analysis 65
5.2.4 Detection threshold determination: 66
5.3 Results and discussion 67
5.3.2 Block paradigm 67
5.3.2 Event-related paradigm 70
5.4 Conclusions 73

VI. CONCLUSION 75

6.1 Numerical evaluation of optimal detection parameters 75
6.2 GABA measurements at 3 Tesla and 7 Tesla 76
6.3 Changes in metabolite profile during neuronal activation 77

6.4 Future directions 78

APPENDIX 80

APPENDIX A. EXAMPLES 80

Appendix A.1 80
Appendix A.2 80
Appendix A.3 82
Appendix A.4 84

APPENDIX B. SUPPLEMENTARY MATERIAL 86

Appendix B.1 86
Appendix B.2 86

REFERENCES 88

LIST OF TABLES

Table 3.1. Metabolite concentrations used in simulations. 29

Table 3.2 CLRBs for PRESS acquisitions at 30 and 109 ms between T2 bounds of 109 and 158 ms. 32

Table 3.3. Linear (y = ax + b) fit of CRLB (y) versus linewidth (x) centered at TE = 109 ms. 37

Table 3.4. CRLBs for echo averaging schemes with T2 at 109 ms. 41

Table 4.1. RF amplitude (B1), corresponding pulse duration and pulse bandwidth (BW) of the excitation (spredrex) and refocusing (gtst1203) pulses used in the study. 51

Table 4.2. RF amplitudes, RF bandwidths and corresponding percent if chemical shift displacement errors in the voxel direction for a refocusing slice-selective pulse..... 58

LIST OF FIGURES

Figure 1.1. Spectral lines generated from simulation of weakly coupled 2-spin system with the chemical shifts of 2ppm and 4ppm and J-coupling of 6Hz. 3

Figure 1.2. Recovery of longitudinal magnetization following 90 degree r.f. pulse. 5

Figure 1.3. Exponential decay of the transverse magnetic field due to T_2 relaxation. 6

Figure 1.4. Timing diagram of PRESS pulse sequence with an echo-time of TE 8

Figure 1.5. MEGA-PRESS J-difference editing pulse sequences. 9

Figure 1.6. Simulated spectra for weakly coupled 2 spin system for MEGA-PRESS with editing pulse applied at 1.9ppm (top), editing pulse off (middle) and the difference spectrum (bottom). 11

Figure 2.1. *In vitro* (blue) and simulated (red) glutamate spectra acquired at 3 Tesla with PRESS sequence at an echo-time of 73 ms. The simulated spectrum was generated using ideal pulses. 18

Figure 2.2. Composite spectrum for 7 Tesla generated from 17 individual metabolite spectra simulated using ideal pulses in C++ with GAMMA libraries. The spectra were simulated for PRESS pulse sequence at an echo-time of 73 ms. 21

Figure 2.3. Schematic diagram showing the basis set generation and analysis process ... 23

Figure 2.4. Output from LCModel analysis showing bottom panel with *in vivo* data and baseline estimation in black, LCModel fit in red and top panel with the residual spectrum. 25

Figure 3.1. Dependence of metabolite lower bounds of precision (CRLBs) on echo-time for T_2 = 109 ms. 32

Figure 3.2. *In vivo* spectrum shown with 3 spectral bases (glutamine, glutamate, inositol) at the echo time optimum for Gln and Glu (109 ms). 34

Figure 3.3 Dependence of metabolite lower bounds of precision (CRLB) on resolution for T_2 = 109 ms 4 to 24 Hz. 37

Figure 3.4. CRLBs of glutamate (left), glutamine (center), and inositol (right) as a function of resolution (FWHM) and echo time at a proton frequency of 300 MHz (7 Tesla). Isolines for 5 and 10% CRLB are shown in blue and purple. 38

Figure 3.5. Metabolite CRLBs in projected 2-d sequences. These curves represent the CRLB of echo-time averages where the starting echo series ranges from 45 to 100

ms in 1 ms increments. For example, the first point includes the CRLB from echoes over the range from 45-100 ms, whereas the last point spans 100-120 ms. 40

Figure 3.6. The dependence of concentration on basis set composition. When 2-hydroxyglutarate is physically present but not used in the fitting for quantification, the concentration of glutamate, glutamine, and γ-aminobutyric acid are overestimated (gray trace) relative to input concentrations (black trace). 42

Figure 4.1. MEGA-PRESS J-difference editing pulse sequences. 46

Figure 4.2. Pulse profile (top) and frequency response (bottom) for a) excitation pulse and b) refocusing pulse used in the study. 50

Figure 4.3. Even (top) and J-difference (bottom) spectra acquired at 3 Tesla (left) and 7 Tesla (right) using MEGA-PRESS sequence at TE = 73 ms with editing pulse bandwidth of 0.5 ppm toggled between 7.4 and 1.9 ppm on even and odd spectra respectively acquired from a 40x30X15 mm^3 voxel from anterior cingulated cortex. 53

Figure 4.4. Comparison of metabolite-to-tCr ratios averaged from even analysis of 11 data sets acquired at 3 Tesla and 7 Tesla. 54

Figure 4.5. Comparison of metabolite-to-NAA ratios averaged from j-difference analysis of 11 data sets at 3 Tesla and 7 Tesla..... 55

Figure 4.6. Comparison of metabolite-to-tCr ratios averaged from even analysis of 4 data sets acquired with RF amplitudes of 15, 16.5 and 18 μT. 56

Figure 4.7. Comparison of metabolite-to-NAA ratios averaged from even analysis of 4 data sets acquired with RF amplitudes of 15, 16.5 and 18 μT..... 57

Figure 5.1. Schematic diagram of the binning method for event-related paradigm, where the scan consisted of m functional cycles and each functional cycle consisted of n time points. t_{ij} represents j^{th} data collected after the onset of stimulation during i^{th} functional cycle. 65

Figure 5.2. (Top) Water peak height (blue) and water line widths (red) during activation and rest blocks. (Bottom)Water spectra acquired during 3 cycles of 30 seconds of activation (red) followed by 30 seconds of rest (blue) showing BOLD response. ... 67

Figure 5.3. In vivo spectra acquired from the visual cortex using MEGA-PRESS sequence with editing frequency at -60 Hz and editing pulse bandwidth of 64 Hz. 120 transients were averaged to generate each spectra at TE/TR = 73/2000 ms..... 68

Figure 5.4. LCModel results for Lactate to Creatine ratio for 7 subjects showing increase in lactate concentration during stimulus (red) compared to rest (blue) for 6 of the 7 volunteers. 69

Figure 5.5. Results from peak analysis showing a) peak height, b) linewidth, and c) area under the NAA peak during activation (red) and rest (blue) for 5 subjects..... 70

Figure 5.6. Metabolite time courses with 2 s resolution during activation (red) and rest (blue) periods averaged across 5 subjects. 71

Figure 5.7. Running average of 5 time points of [lac/tCr] as a function of time from 5 subjects. Red plot represents [lac/tCr] area during 32 s of activation and blue during 32 s of rest. The last 4 points in the plot only consist of data from 1 time point..... 72

LIST OF ABBREVIATIONS

2-HG	2-hydroxyglutarate
Ala	alanine
Asp	aspartate
BW	Bandwidth
Cho	choline
Cre	creatine
CRLB	Cramer-Rao Lower Bounds
CS	Chemical Shift
CSF	Cerebrospinal Fluid
FID	Free Induction Decay
fMRI	Functional Magnetic Resonance Imaging
fMRS	Functional Magnetic Resonance Spectroscopy
FWHM	full-width half-maxumum
GABA	γ-Aminobutyric Acid
Glc	glucose
Gln	glutamine
Glu	glutamate
GPC	glycerophosphoryl-choline
GSH	glutathione
Ins	myo-Inositol
Lac	lactate
MRS	Magnetic Resonance Spectroscopy

NAA	N-acetylaspartate
NAAG	N-acetylaspartylglutamate
PCr	phosphocreatine
PCh	phosphoryl-choline
PRESS	Point Resolved Spectroscopy
RF	radio frequency
SAR	specific absorption rate
Si	scyllo Inositol
SNR	signal-to-noise ratio
STEAM	Stimulated echo
SVD	singular value decomposition
Tau	taurine
TE	echo-time
TR	repetition time

CHAPTER I

INTRODUCTION

1.1 Nuclear magnetism

Magnetic resonance spectroscopy (MRS) is a non-invasive technique that can be used to quantify various chemicals and identify molecular structures. MRS relies on the existence of a net magnetic moment of nuclei with either odd protons or neutrons. A nucleus with spin I can have (2I + 1) energy levels that are quantized and separated by ΔE.

$$\Delta E = \frac{\mu B_o}{I} \tag{1.1}$$

So for a spin ½ there are two possible states: +½ and -½. In the presence of an external magnetic field, the magnetic dipole moment (μ), if oriented at an angle to the applied field, experiences torque (τ) and precesses about the applied field.

$$\vec{\tau} = \vec{\mu} X \vec{B} \tag{1.2}$$

The interaction Hamiltonian of the spin with applied magnetic field is given by:

$$H_z^I = -\gamma\hbar \mathbf{I} \cdot (\mathbf{1} - \sigma_I) \cdot \mathbf{B}_0 \tag{1.3}$$

This is referred to as the Zeeman Hamiltonian and is frequently expressed in angular frequency units (divide through by $\hbar$). γ is the gyromagnetic ratio which is unique to different nuclei, for Hydrogen, γ = 42.6MHz/Tesla. The $\boldsymbol{\sigma}_I$ term in each of these expressions refers to the chemical shift of the spin I.

Chemical shifts are often described as being more or less shielded or upfield and downfield, respectively. Shielding is theoretically measured with respect to a bare nucleus (a difficult circumstance to create) and simply means that the magnetic field, B_0,

is effectively reduced at the nucleus due to the interaction of the electrons surrounding the nucleus. The chemical shifts and spin-spin couplings (J-couplings) of different chemicals give rise to a spectrum that is characteristic of that particular chemical. J-couplings are the couplings between two spins that are mediated by the bonding electrons. Spectra of specific metabolites can be used to obtain information on chemical shifts and j-couplings as well as the chemical structure of the metabolites. The concept behind the generation of the spectrum in the context of one spin and two weakly coupled spin systems are discussed below.

The eigenvalue equations for the single-spin Hamiltonian (Eq. 1.3) are:

$$H_Z^I \left|+/-\right\rangle = \pm\left(\frac{\omega_I}{2}\right) \left|+/-\right\rangle \tag{1.4}$$

where $\omega_I = \omega_0(1-\sigma_I)$ and is called the Larmor frequency, the precession frequency of the spin under the influence of a static magnetic field, B_0, and ω_0 is the natural precession frequency in the absence of chemical shielding. In these expressions, $\left|+\right\rangle$ and $\left|-\right\rangle$ refer to states parallel and anti-parallel to $B_0 \cdot \mathbf{z}$, respectively, and it follows that (with this convention) the $\left|+\right\rangle$ state is lower in energy than the $\left|-\right\rangle$ state. The energy associated with the transition between the two states is:

$$\Delta E_{\pm} = \left(E_- - E_+\right) = \omega_0(1-\sigma_I) = \omega_I \tag{1.5}$$

This energy is simply the interaction energy of the spin with the static field, where the field has been scaled by the chemical shift.

The Hamiltonian for a weakly coupled 2 spin system in the eigenbasis is given by:

$$H = H_Z^I + H_Z^S + H_J^{IS}, \tag{1.6}$$

where $$H_J^{IS} = JI_{IZ}.I_{SZ}$$

and the corresponding eigenvalue equations are:

$$\begin{aligned} H_Z\left|+_I;+_S\right\rangle &= (-\tfrac{1}{2}\left(\omega_I+\omega_S\right)+J/4)\left|+_I;+_S\right\rangle \\ H_Z\left|+_I;-_S\right\rangle &= (-\tfrac{1}{2}\left(\omega_I-\omega_S\right)-J/4)\left|+_I;-_S\right\rangle \\ H_Z\left|-_I;+_S\right\rangle &= (+\tfrac{1}{2}\left(\omega_I-\omega_S\right)-J/4)\left|-_I;+_S\right\rangle \\ H_Z\left|-_I;-_S\right\rangle &= (+\tfrac{1}{2}\left(\omega_I+\omega_S\right)+J/4)\left|-_I;-_S\right\rangle \end{aligned} \tag{1.7}$$

The transition probabilities and the corresponding transition energies are:

$$\begin{aligned} |<+_I;+_S\,|\,J^+\,|\,-_I;+_S>|^2 = 1 &\longrightarrow \Delta E = -\omega_I + J/2 \\ |<+_I;+_S\,|\,J^+\,|\,+_I;-_S>|^2 = 1 &\longrightarrow \Delta E = -\omega_S + J/2 \\ |<-_I;+_S\,|\,J^+\,|\,-_I;-_S>|^2 = 1 &\longrightarrow \Delta E = -\omega_S - J/2 \\ |<+_I;-_S\,|\,J^+\,|\,-_I;-_S>|^2 = 1 &\longrightarrow \Delta E = -\omega_I - J/2 \end{aligned} \tag{1.8}$$

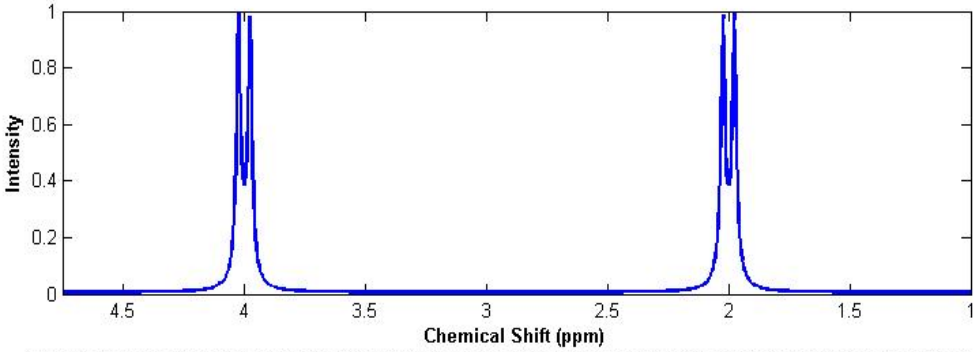

Figure 1.1. Spectral lines generated from simulation of weakly coupled 2-spin system with the chemical shifts of 2ppm and 4ppm and J-coupling of 6Hz.

The generalized Hamiltonian for the spin systems are:

$$\begin{aligned} &H_Z^i = \gamma_i \mathbf{B}_0\left(1-\sigma_i\right)\mathbf{I} = \omega_i I_{iz} \\ &and \\ &H_J^{ij} = J\mathbf{I}_i \cdot \mathbf{I}_j \end{aligned} \tag{1.9}$$

where H_Z^i represents the individual spin Hamiltonian and H_J^{ij} represents the J-coupling Hamiltonian. As we can see from Eq. 1.9, as the number of spins increase, the

Hamiltonian and hence the calculation of the eigenvalues becomes significantly complicated.

1.2 Effect of radio frequency (RF) field on the spin in magnetic field

When an RF pulse is applied with the correct frequency and bandwidth to affect the desired spin, the spin experiences two magnetic fields: the static magnetic field (B_0) and the oscillating RF field (B_1) from the excitation coil. The equations governing the spin dynamics in the presence of these two fields in a frame that is rotating at a frequency ω are given by (*1*)

$$B_{eff} = \sqrt{(B_0 - \omega / \gamma)^2 + B_1^2} \tag{1.10}$$

and the effective Hamiltonian when B_1 is along x-axis is given by:

$$H_{eff} = H_Z + \gamma B_1 I_x \tag{1.11}$$

The RF field is several orders of magnitude smaller than the static field but as seen from Eq. 1.12, when B_1 is on resonance, the spin will precess about the applied field. The flip angle as a result of the B_1 is $\gamma B_1 t$, where t is the duration of the applied field. The effect of the j-coupling on the spins can be understood by using the following commutation relations (*1*).

$$\begin{aligned}
\left[2\hat{I}_{1z}\hat{I}_{2z}, \hat{I}_{1x}\right] &= i2\hat{I}_{1y}\hat{I}_{2z} \\
\left[2\hat{I}_{1z}\hat{I}_{2z}, \hat{I}_{2x}\right] &= i2\hat{I}_{1z}\hat{I}_{2y} \\
\left[2\hat{I}_{1x}\hat{I}_{2z}, \hat{I}_{1y}\right] &= i2\hat{I}_{1z}\hat{I}_{2z} \\
\left[2\hat{I}_{1z}\hat{I}_{2x}, \hat{I}_{2y}\right] &= i2\hat{I}_{1z}\hat{I}_{2z}
\end{aligned} \tag{1.12}$$

The knowledge of these transformations and the resulting operators has been used to devise pulse sequences to maximize the signal from various spin systems. $\hat{I}_x$, $\hat{I}_y$ and $\hat{I}_z$

are the angular momentum operators. The product operator analysis of some of the pulse sequences like PRESS and MEGA-PRESS are shown below.

1.3 Relaxation processes

Longitudinal relaxation or spin-lattice relaxation is the recovery of the component of magnetization along the axis of the static field after 90^{o} pulse, usually denoted along z-direction (M_z) and is characterized by the longitudinal relaxation rate (T_1).

$$M_z(t) = M_0(1 - e^{-t/T_1}) \tag{1.13}$$

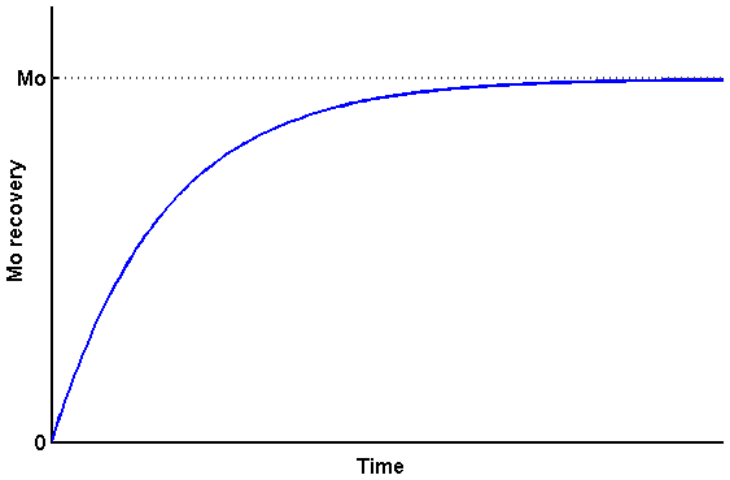

Figure 1.2. Recovery of longitudinal magnetization following 90 degree r.f. pulse.

Transverse relaxation or spin-spin relaxation is the loss of magnetization along the axis perpendicular to the static field (x and y axes) and is characterized by the transverse relaxation rate (T_2). Transverse relaxation occurs due to the loss of phase coherence of the spins in the x-y plane due to the fluctuations in the local magnetic fields (dipolar interactions) and hence, the effective magnetic field experienced by the spins. Transverse relaxation can be observed as an exponential decay in the signal.

$$M_{xy} = M_0 e^{-t/T_2} \tag{1.14}$$

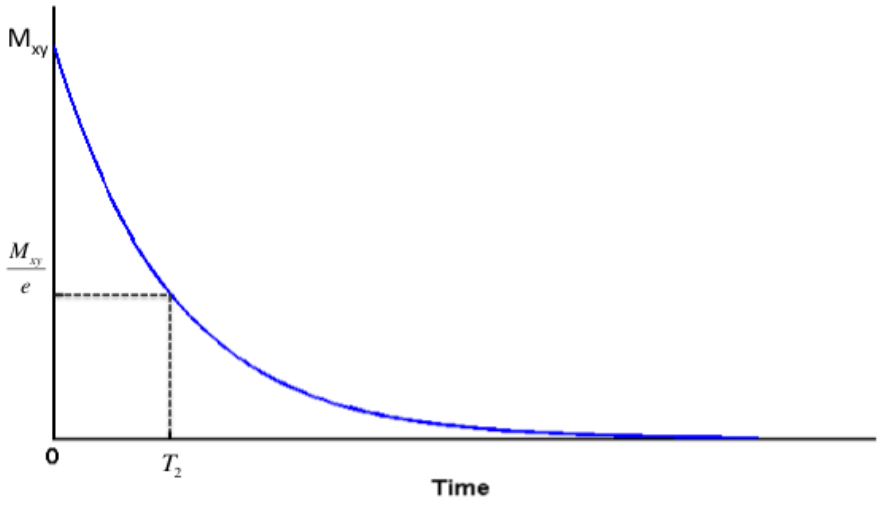

Figure 1.3. Exponential decay of the transverse magnetic field due to T_2 relaxation.

1.4 Localization

Localization in NMR spectroscopy is achieved by applying a sequence of frequency-selective RF pulses in the presence of a B_0 field gradient. The thickness of the region of interest along each direction is controlled by the bandwidth (BW) of the RF pulse and the B_0 field gradient (G_i) and follows the following relationship:

$$x = \frac{BW}{\gamma G_x} \tag{1.15}$$

where x is the size of the voxel in x-axis, BW is the bandwidth of the RF pulse and G_x is the slope of the gradient applied in the direction of localization, x-axis in this case. When the frequency selective RF pulse is applied in conjunction with linear B_0 field gradient to only affect a slice of a volume it is called a slice-selective pulse. Single voxel localization is accomplished by the application of these slice-selective pulses in three directions in sequence such that only spins in a limited volume experience the intended

rotation of the spins resulting in the observable signal generation from that particular volume.

The difference in Larmor frequency ω_0 that aids in the discrimination of metabolites leads to the spatial displacement Δx of the localized volume between different metabolites:

$$\Delta x = \frac{\Delta \omega}{BW_{rf}} x \tag{1.16}$$

where x is the size of the voxel, $\Delta\omega$ is the difference in chemical shift between to protons, BW_{rf} is the bandwidth of the RF pulse, Δx is the chemical shift displacement in voxel direction (*2*).

1.5 Pulse sequences

Three dimensional localization pulse sequences like Point Resolved Spectroscopy (PRESS) and Stimulated-echo Acquisition Mode (STEAM) are two of the widely available pulse sequences on standard human MRI scanners.

PRESS

PRESS sequence is a double spin echo sequence that consists of an initial 90^o pulse that tips the net magnetization in the transverse plane, followed by two 180^o pulses to refocus chemical shift evolution and free induction decay signal acquired at the end of the echo time. The pulse-timing diagram for PRESS pulse sequence is given in Figure 1.4. The application of the initial 90^o excitation pulse tips the net magnetization in the transverse plane and the spins undergo chemical shift and j-coupling evolution for time TE_1 until the application of 180^o pulse, which inverts the net magnetization and the

chemical shift evolution begin to refocus with a spin echo being formed after the delay TE_1 where the chemical shift evolution is completely refocused. The spins continue to evolve during the first TE_2 delay until the second 180^o pulse refocuses the chemical shift evolution that occurred during the TE_2 delay with the second spin echo being formed after duration TE_2 after the second 180^o pulse. For an IS spin system, the resulting product operator is given below:

$$\begin{aligned} I_z &= -I_y \cos\{\pi JTE\} + 2I_x S_z \sin\{\pi JTE\} \\ S_z &= -S_y \cos\{\pi JTE\} + 2I_z S_x \sin\{\pi JTE\} \end{aligned} \tag{1.17}$$

For the given pulse timings, chemical shift evolution is refocused at the end of the echo-time as we can see from the resulting terms in the product operator.

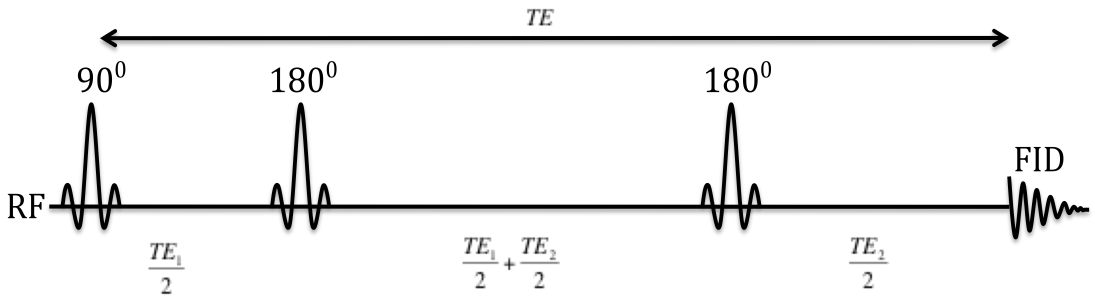

Figure 1.4. Timing diagram of PRESS pulse sequence with an echo-time of TE

These pulse sequences can be modified by addition of pulses to acquire data from specific spin systems that are otherwise difficult to detect and quantify. One example of such modified pulse sequence is MEGA-PRESS sequence, which consists of two additional frequency-selective pulses.

MEGA-PRESS

MEGA-PRESS is a frequency selective refocusing technique that was proposed by Mescher et al in 1998 as a way to simultaneously suppress water and perform spectral

editing. MEGA-PRESS is widely used to acquire J-difference spectra for metabolites like γ-Aminobutyric Acid (GABA) (*3, 4*) and Glutathione (GSH) (*5*), which, are difficult to quantify due to the presence of overlapping resonances on spectra acquired without any editing (*3*). MEGA-PRESS consists of two additional frequency selective pulses the first of which is placed between the two refocusing pulses of PRESS sequence and the second is placed after the second refocusing pulse. The second modification in the MEGA-PRESS sequence from PRESS sequence is the rearrangement of the second set of crusher gradients. These gradients are rearranged to dephase only those spins that experience the additional refocusing pulses.

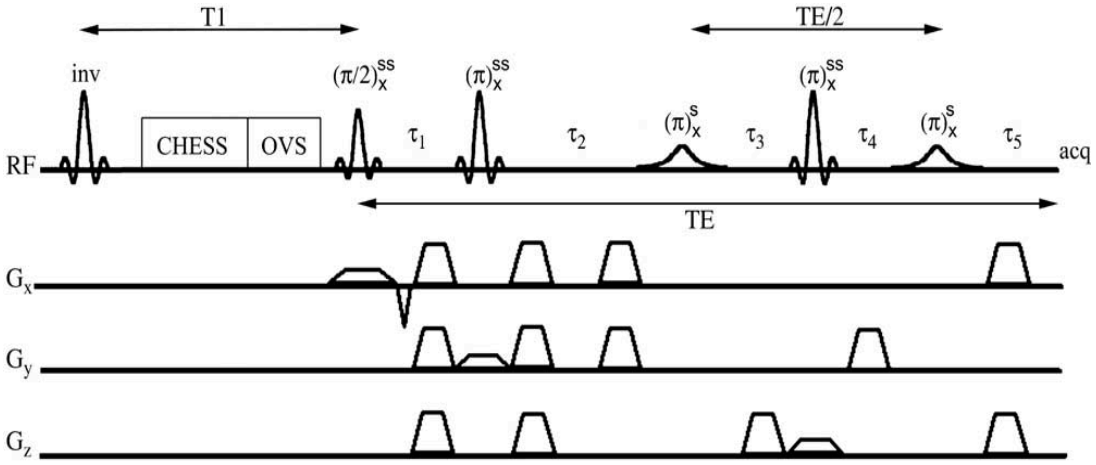

(Waddell et al 2007)

Figure 1.5. MEGA-PRESS J-difference editing pulse sequences.

Editing pulse on:

$$I_z \rightarrow -I_y \cos\{\pi J_{IS}(t_1+t_2-t_3-t_4+t_5)\} + 2I_xS_z \sin\{\pi J_{IS}(t_1+t_2-t_3-t_4+t_5)\}$$
$$S_z \rightarrow -S_y \cos\{\pi J_{IS}(t_1+t_2-t_3-t_4+t_5) + 2I_zS_x \sin\{\pi J_{IS}(t_1+t_2-t_3-t_4+t_5)\} \quad (1.18)$$

We can see from the resulting product operator that as long as the timing below is satisfied, the spins coupled to the spins refocused by the additional frequency selective pulses are independent of time and purely absorptive as long as: $t_1 + t_2 - t_3 - t_4 + t_5 = 0$. Also, since $t_1 + t_2 + t_5 = t_3 + t_4$ from PRESS sequence, and it follows that:

$$\begin{aligned} t_1 &= shortest \\ t_2 &= \frac{TE}{4} \\ t_4 &= \frac{TE}{4} \\ t_5 &= \frac{TE}{2} - t_1 - t_2 \\ t_3 &= \frac{TE}{2} - t_4 = \frac{TE}{4} \end{aligned} \tag{1.19}$$

Editing pulse off:

$$\begin{aligned} I_z &\rightarrow -I_y \cos\{\pi J_{IS}(t_1 + t_2 + t_3 + t_4 + t_5)\} + 2I_x S_z \sin\{\pi J_{IS}(t_1 + t_2 + t_3 + t_4 + t_5)\} \\ S_z &\rightarrow -S_y \cos\{\pi J_{IS}(t_1 + t_2 + t_3 + t_4 + t_5) + 2I_z S_x \sin\{\pi J_{IS}(t_1 + t_2 + t_3 + t_4 + t_5)\} \end{aligned} \tag{1.20}$$

Resulting difference observable operators (on – off) after using trigonometric identity for cosine:

$$2I_y\{\sin\{\pi J_{IS}(t_1 + t_2 + t_5)\}\sin\{\pi J_{IS}(t_3 + t_4)\} + 2S_y\{\sin\{\pi J_{IS}(t_1 + t_2 + t_5)\}\sin\{\pi J_{IS}(t_3 + t_4)\} \tag{1.21}$$

An example of spectra acquired during on and off acquisitions along with the j-difference spectra is shown in figure 1.6.

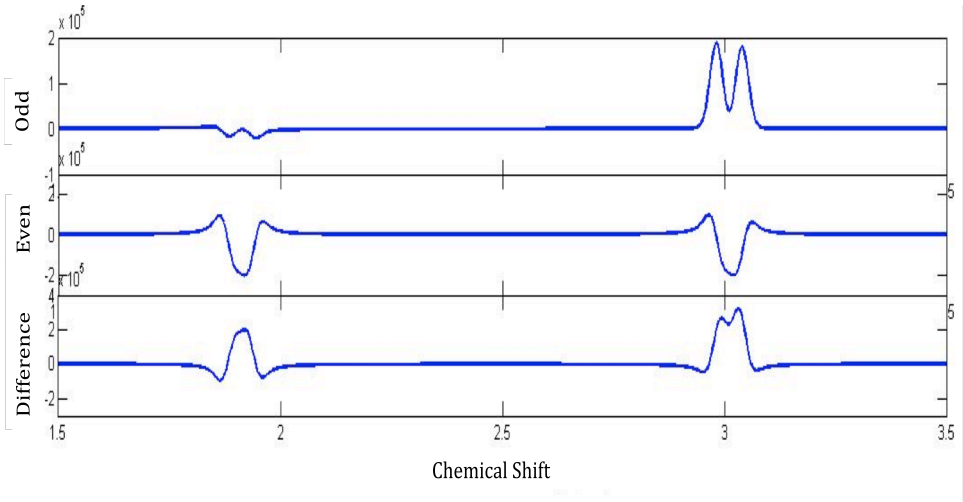

Figure 1.6. Simulated spectra for weakly coupled 2 spin system for MEGA-PRESS with editing pulse applied at 1.9ppm (top), editing pulse off (middle) and the difference spectrum (bottom).

1.6 Practical considerations

Signal-to-noise

The signal-to-noise ratio (SNR) of metabolites is directly proportional to the voxel size, static magnetic field (B_0), the square root of the number of acquisitions and the concentration of the metabolite of interest. The concentration of water in the brain is much higher than the concentration of metabolites (50M vs. 1-15mM) such that metabolite measurements cannot be made without either suppressing the water signal during data acquisition or using singular value decomposition (SVD) to subtract the water signal during post-processing phase. The low concentration (mM levels) of metabolites in the human brain the signal-to-noise ratio (SNR) from a single shot is not enough to make metabolite concentration measurement. Therefore, a number of transients are acquired and averaged together in order to achieve high enough SNR to quantify concentrations.

Baseline

One of the issues that need to be handled carefully for accurate quantification is baseline fluctuation. The origin of baseline is believed to come from macromolecules and residual signal from water. The residual signal from water can be approximated as an exponential decay and the baseline contribution from macromolecules appear as a set of broad peaks due to short T2 relaxation of the macromolecules. The spectral contribution from macromolecules have been studied by various groups (*6, 7*) among which the results obtained by Behar's paper is likely one of the most detailed and careful studies conducted to characterize the chemical shifts and j-couplings on macromolecule spectra. Mishandling of the baseline fluctuations can result in the incorrect quantification of metabolites. Hence, some quantification tools include a semi-parametric fitting of the baseline by incorporating prior knowledge of the baseline contribution from residual water signal and macromolecule spectrum. One of the approaches to approximate the baseline has been to acquire 'metabolite-nulled' spectrum to be used as part of the basis set during metabolite quantification. However, due to the differences in longitudinal relaxation rates of the metabolites, acquisition of a truly metabolite-nulled spectrum is difficult and the acquired spectrum is contaminated by residual peaks from the metabolites with different inversion-recovery rates during spectra acquisition causing further error in the analysis. A way to circumvent the issue is to use pulse-sequences that allow the use of non-parametric methods like MEGA-PRESS. MEGA-PRESS is widely used for making GABA measurements by selectively refocusing the coupled resonance of interest on alternate scans and subtracting the two scans. This effectively removes the baseline from the resulting spectra and results in a more manageable spectrum to analyze.

B_0 inhomogeniety

The increase in the strength of the static magnetic field has the added benefit of increased SNR and spectral resolution, however, increase in B_0 also bring with it some challenges. A homogeneous static magnetic field is one of the requirements of acquiring spectrum of good quality and as we go to higher fields it becomes harder to achieve reducing our ability to discriminate between different resonances. B_0 homogeniety influences the Larmor frequency of the protons hence, an inhomogeneous static magnetic field causes a distribution of Larmor frequency from the same metabolite. This, in turn, causes the pulses applied to effect the signal coming from a particular metabolite to be effected differently by the same pulse and ultimately cause incoherent signal averaging as well as result in signal that deviate from the expectation from prior knowledge for signal generated from a homogeneous field. The preparation phase of the scan includes a process to homogenize the static magnetic field and is called shimming.

B_1 inhomogeniety

One of the challenges in acquiring high quality spectra arises from B_1 inhomogeneity. The attenuation and interference of radio waves and absorption of radiation in the tissue increases as we go to higher fields. The frequency of the transmitted RF radiation needs with increase in B_0 leading to an increase in the degree of RF attenuation in a dielectric medium such as the human body. Also, at the emerging field strength of 7 Tesla, the RF wavelengths decrease to ~ 10 cm, roughly the dimension of the human head. As the dimension of the RF wavelengths in the dielectric medium approach the sample dimension, standing waves are generated in the sample causing spatially varying B1 field

being experienced across the sample. This generates problems with the depth of RF penetration of the body along with varying RF amplitude delivery across the selected volume (*8*). The methods used to reduce B_1 inhomogeniety are the use of B_1 insensitive pulses and multi-transmit coil.

CHAPTER II

SIMULATION AND QUANTIFICATION OF NEUROTRANSMITTER MEASUREMENTS BY MRS

2.1 Simulated basis set

In vivo MRS of the brain is aimed at acquiring information about various metabolites, their intermediates, and their levels in normal subjects as well as subjects with various disorders. Quantitative measurement of the concentrations of metabolites can be used to establish the normal levels in healthy subjects and to study the changes that occur in diseases (*9-12*). MRS may also be used to investigate the energetic basis of brain activity studying the changes in metabolic profile during regional activation (*13, 14*) and modeling these changes also demands precise quantification of metabolites. Various quantification techniques are used to measure the metabolite concentrations from spectra obtained *in vivo,* most of which rely on prior knowledge.

The spectra of individual compounds may be acquired from *in vitro* experiments or predicted from simulation and these form a basis set by which experimental spectra can be fitted. Acquisition of individual *in vitro* metabolite spectra for use as a basis set demands highly controlled parameters to avoid contamination of solutions and ensure temperature and pH that mimic *in vivo* conditions. It also requires careful monitoring of the integrity of the solutions prior to acquisition of spectra since the solutions can degrade over time. It can also be highly tedious to acquire in vitro spectra for different echo times and pulse sequences for all the different metabolites of interest at different static magnetic field strengths.

Use of simulated spectra, on the other hand, can be a much quicker and more reliable approach if the chemical shifts and J-coupling constants of the metabolites are known (*15*). The information available on the spin systems of metabolites of interest can be used to study the effects of pulse sequence and echo-times on the resulting spectra using numerical simulations. Packages like JMRUI and GAMMA libraries in C++ can be used to simulate spectra for different pulse sequences and to predict complex spectra for mixtures of different metabolites (*16, 17*). Apart from the efficiency of basis set generation, simulated basis set have the added benefit of having narrow linewidths and having infinite SNR since simulated spectra are free of noise. Hence, simulated basis sets allow for more precise and accurate quantification and having an accurate basis set is key to accurate quantification of metabolites.

Efficient generation of simulated basis set for quantification of metabolites involves writing programs to perform density matrix simulations of the evolution of spins as a function of applied RF pulses, normalizing the simulated spectra and formatting the normalized spectra for use with the quantification tool of choice, which in our case is LCModel. This chapter details the basis set generation process we have built and used for generating basis sets for analyzing the experimental data sets and for optimizing the metabolite detection echo-time as part of this thesis.

2.2 Density Matrix Simulations

GAMMA libraries, written in C++, aid in performing density matrix calculations and can be used to perform density matrix simulations using ideal or real pulses for individual metabolites for a specified pulse sequence (*17*). GAMMA libraries consist of

sub-routines for performing individual spin and spin system operations and can be used to design and run full density matrix simulations for any pulse sequence. GAMMA libraries require information such as nucleus, chemical shift, j-couplings of the spin system of interest, and static magnetic field strength (B_0) as inputs. C++ programs can be written to specify the parameters to be used for simulations such as pulse sequence design, pulse types and echo-time. An example of spin system specification for a system with 2 spins with a J-coupling of 7 Hz is shown in Appendix A.1.

Once the spin information is passed to the program, the density matrix for a system in equilibrium is generated. As the system is perturbed by the RF-pulses, the density matrix evolves under the effect of the perturbation.

$$\hat{\sigma}(t + t_0) = e^{-i\hat{H}t}\sigma(t_0)e^{i\hat{H}t}$$

where $\hat{\sigma}(t + t_0)$ is the density matrix after evolution under the influence of acting Hamiltonian $\hat{H}$ and $\hat{H} = H_0 + H_{rf}$.

Spin simulations for systems with larger numbers of spins require large matrix sizes to be computed and the density matrix simulations become significantly slower for spins with 8 or more spins. In these cases, splitting spin systems into smaller systems while grouping coupled spins as one spin system and running density matrix simulations has been proven to restore the efficiency. For metabolites like choline, phosphoryl choline and glycerol-phosphocholine that consist of 13, 13 and 18 spins respectively with 9 spins each that are singlets, splitting the spin systems is an ideal solution. An example of a program that illustrates the Point Resolved Spectroscopy (PRESS) sequence with ideal pulses is given in Appendix A.2.

The GAMMA package also includes sub-routines that facilitate applying real pulse shapes to be incorporated in simulations in order to study the effect of RF-field strength, pulse shapes and bandwidths in the resulting spectrum. A program that illustrates PRESS sequence with real pulses is given in Appendix A.3. An example showing close agreement between an experimentally measured *in vitro* glutamate spectrum and a simulated glutamate spectrum is shown in Figure 2.1.

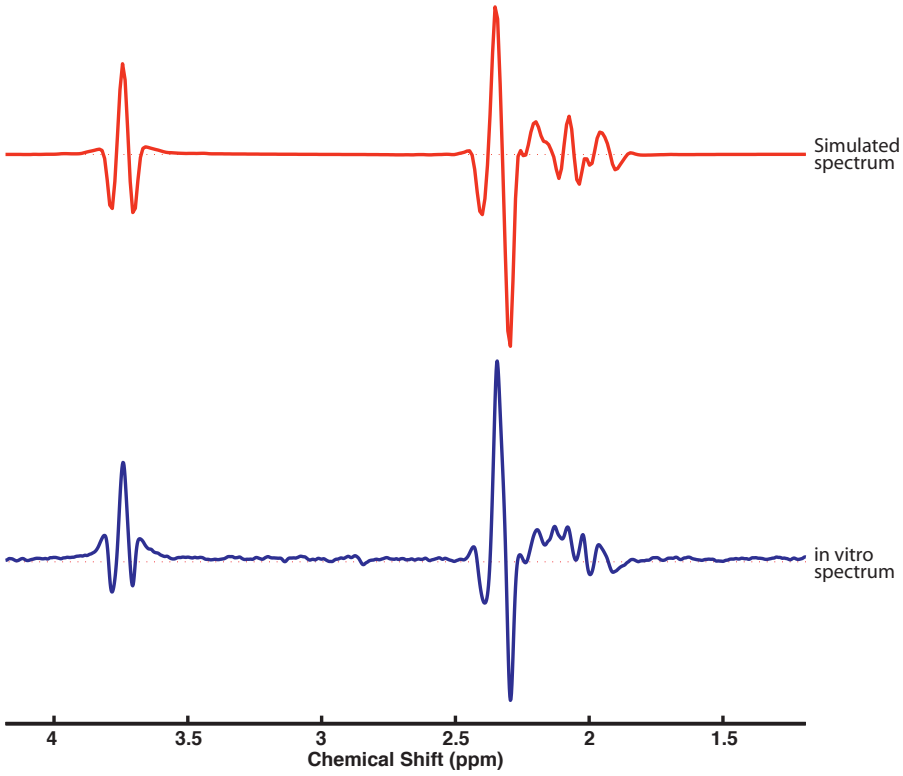

Figure 2.1. *In vitro* (blue) and simulated (red) glutamate spectra acquired at 3 Tesla with PRESS sequence at an echo-time of 73 ms. The simulated spectrum was generated using ideal pulses.

2.3 Normalizing the simulated spectrum

The resulting time-domain signals from the GAMMA simulations need to be normalized to allow quantitative evaluation of spectra. In the correct representation of the

spectrum, the spectra should scale linearly as a function of the number of spins such that the area under a singlet peak from 2 spins should be twice that under a singlet peak from 1 spin. However, the output from GAMMA simulations is scaled according to an exponential function based on the number of spins in the spin system and needs to be accurately normalized. This issue is addressed by adding a singlet resonance at 15 ppm, away from any of the metabolite resonances in the brain, as part of the spin system of interest. The density matrix calculations are performed on the spin systems that include the reference peak that is used to correct the phase of the spectrum as the first step after the completion of density matrix simulations. The second step entails correcting for any baseline fluctuation in the reference peak, due to the influence of the metabolite resonances, by fitting a line between 14 ppm and 16 ppm spectral window and subtracting the baseline from the peak. The third step is calculating the area under the reference peak after baseline subtraction and normalizing the area to 1 for all metabolites and saving the resulting spectra as .SDAT and .SPAR files. .SDAT files contain the free induction decay signal (FID) and .SPAR files contain the acquisition parameters in the format compatible for MRS data from a Philips MR scanner.

The accuracy of the normalization of the simulated spectra is crucial for the spectra to be useful in analyzing experimental data; hence even the slightest baseline fluctuation contribution from metabolite resonances far from the reference peak needs to be subtracted. The results from quantification of metabolite concentrations will be less accurate if analyzed using inaccurately normalized or randomly scaled spectra as prior-knowledge.

2.4 Quantification

Some of the methods for quantifying metabolite concentrations from an experimental spectrum include calculating the area under the metabolite peaks or fitting the peaks in the spectrum by using a basis set generated using prior-knowledge. Measurements of metabolite concentrations by calculating the area under the metabolite peaks are feasible in cases where there is a distinct peak from a metabolite without contamination from other metabolite resonances and the SNR is adequate. However, several metabolites of interest like glutamate and glutamine suffer from significant spectral overlap from other metabolites and from each other. In these cases, fitting all the resonances in the spectral window of interest yields a more reliable measure of metabolite concentrations. Quantification results from MRS are often reported as ratios of metabolite with respect to Creatine as the concentration of Creatine is believed to be constant (*18*). Absolute quantification of metabolites can be performed by comparison of metabolite concentrations to known concentrations in samples used as an external reference or by using water signal as an internal reference (*7*).

2.5 LCModel

There are several widely used programs available for analyzing spectra among which LCModel is one standard approach used for quantifying metabolite concentrations (*19*). All the experimental data collected for this thesis were quantified using LCModel. LCModel uses linear combinations of individual metabolite spectra to fit experimental data and minimize the residual noise and output metabolite concentration of the analyzed spectrum. LCModel requires individual metabolite spectra to be used as a basis set for a

given pulse sequence and echo-time for analysis of experimental spectra. Figure 2.2 shows simulated spectra for 17 individual metabolites and the composite spectrum generated using a linear combination of the 17 metabolites spectra at echo-time of 73 ms for PRESS sequence at 7 Tesla with linewidth of 10 Hz. The individual metabolite spectra were simulated using the procedure outlined in the sections above.

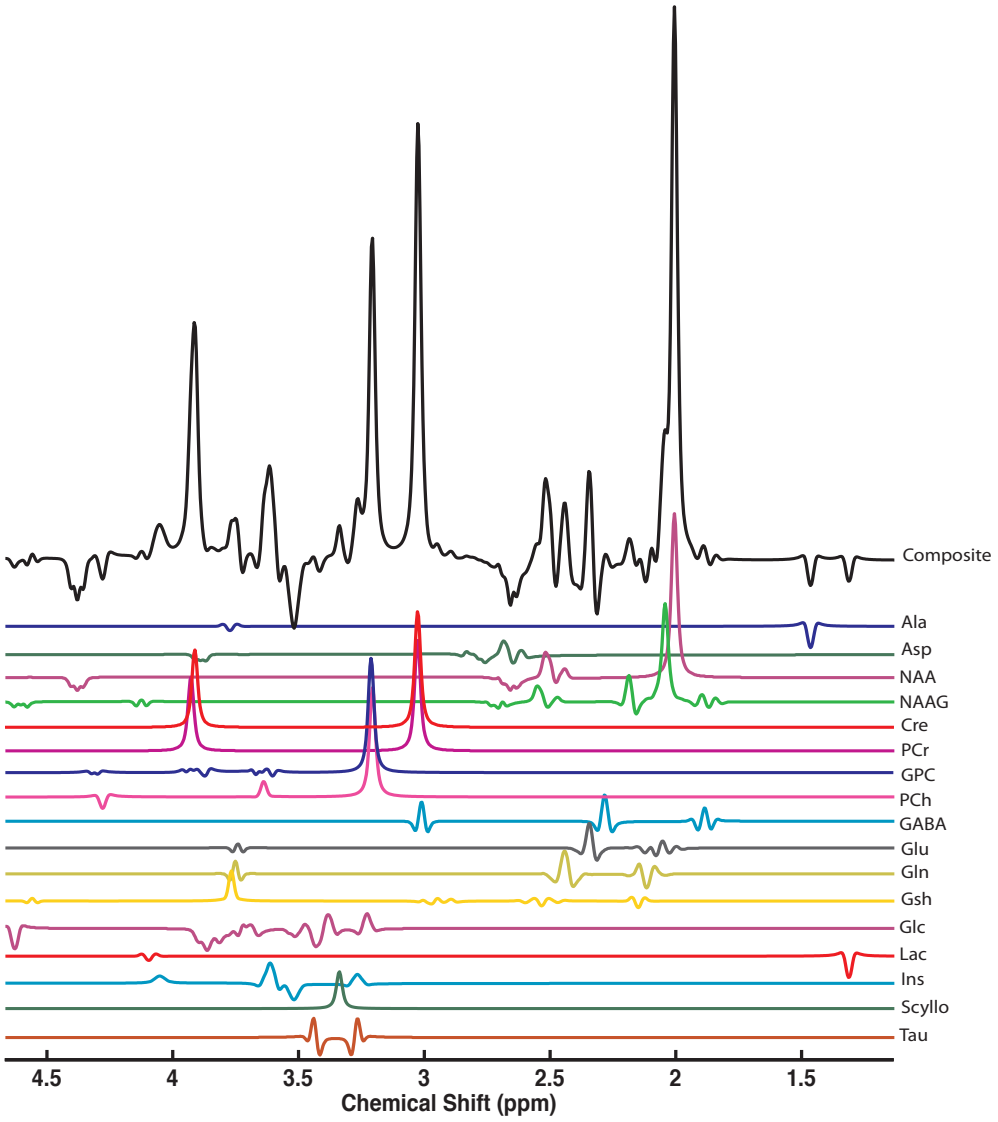

Figure 2.2. Composite spectrum for 7 Tesla generated from 17 individual metabolite spectra simulated using ideal pulses in C++ with GAMMA libraries. The spectra were simulated for PRESS pulse sequence at an echo-time of 73 ms.

2.5.1 Making basis set for LCModel

The individual metabolite spectrum used for analyzing the data for this thesis were generated using programs written in C++ using GAMMA libraries as discussed in section 2.2 and used in conjunction with LCModel to analyze metabolite concentrations. For the generation of LCModel basis set the normalized FID is further saved in a .SDAT, .SPAR and .RAW files as per LCModel requirement using custom built programs written in MATLAB. The next step to making a basis set for LCModel is generating a makebasis.IN file that consists of information on the metabolites, their FIDs and their corresponding concentrations to be used for basis set generation. An example of a *makebasis.IN* file is shown in Appendix A.4.

After the generation of basis set for use with LCModel, all data sets with acquisition parameters such as the pulse sequence and echo-time matching that of basis set can be analyzed using that particular basis set. A schematic diagram showing the basis set generation process and analysis is shown in Figure 2.3.

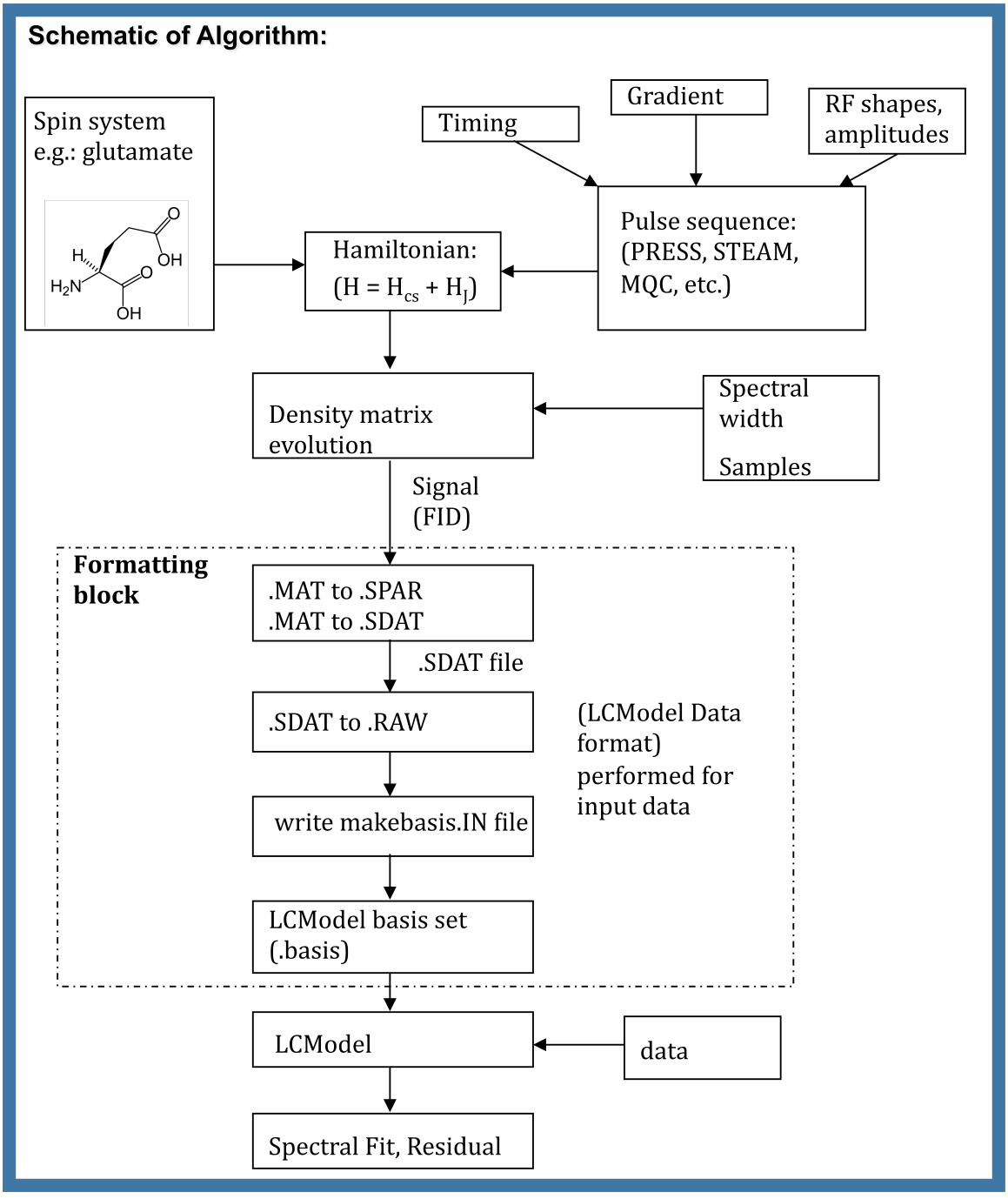

Figure 2.3. Schematic diagram showing the basis set generation and analysis process

It is important for the basis set to have all the metabolites that are present in the data to be quantified in order to avoid a systematic bias in the quantification results.

2.6 Interpreting LCModel Results

As mentioned in the previous chapter, lack of proper understanding and absence of a good model of the baseline in the *in vivo* data pose key limitations in accurate quantification of metabolites concentrations in the human brain. LCModel uses uniform b-spline fits in order to model for the baseline in *in vivo* MR spectra and is a widely accepted practice albeit not a perfect one. LCModel fit uses linewidth and metabolite concentration, phase and frequency shift in the data as some of the parameters that are regularized during the analysis process which yields metabolite concentration, % standard deviations and metabolite-to-creatine ratios. An example of an output from LCModel showing input data, fit results and residual spectrum is shown in Figure 2.4.

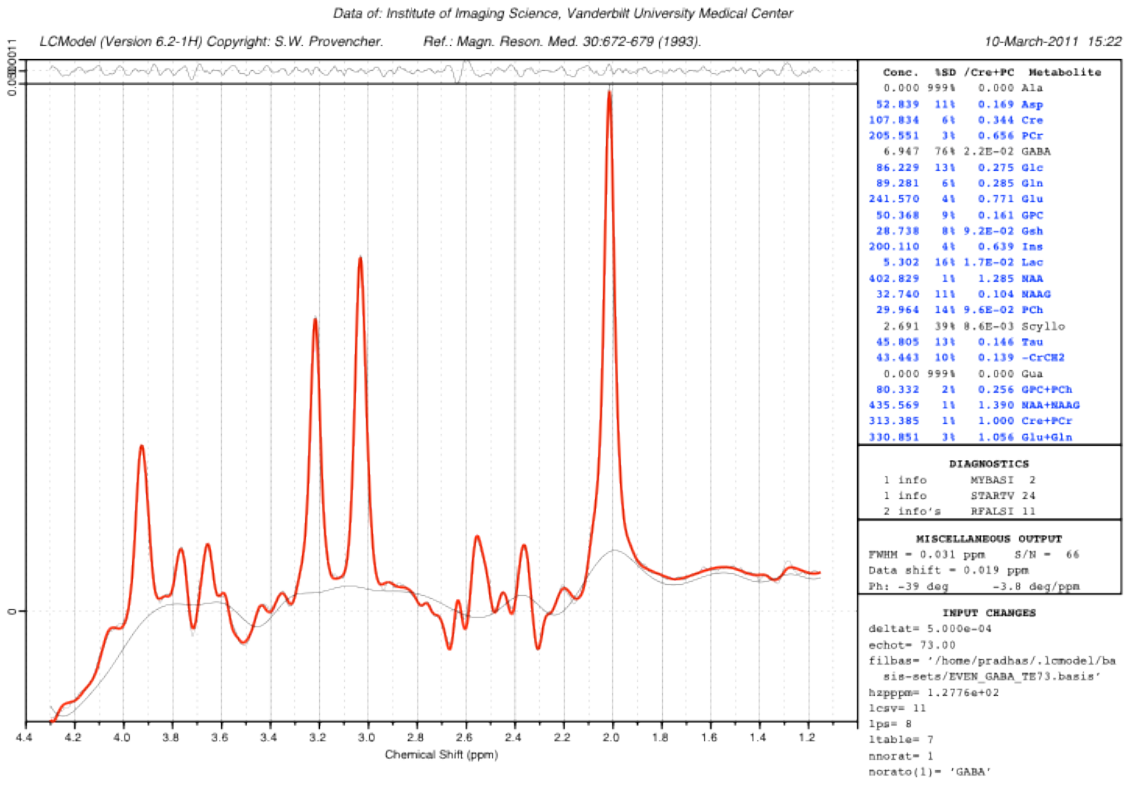

Figure 2.4. Output from LCModel analysis showing bottom panel with *in vivo* data and baseline estimation in black, LCModel fit in red and top panel with the residual spectrum.

The results from LCModel analysis have metabolite-to-creatine ratios and the measurement precision associated with each measurement. The % SD in the output from LCModel analysis is not a traditional standard deviation of the measurement that is reported but the estimate of the lower bound on the measurement precision also called the Cramer-Rao Lower Bounds (CRLB). The results from LCModel analysis represent the nominal precision of the metabolite ratios (*20, 21*) such that the lower CRLBs denote metabolites quantified with higher precision and metabolites with CRLBs lower than 10% from LCModel are widely accepted.

2.7 Cramer-Rao Lower Bounds

CRLB represents the lowest variance of an estimate. CRLB can, therefore, give an estimate of the best measurement precision achievable for the given set of parameters like echo-time, pulse sequence, SNR, linewidths, etc. There have been studies aimed at assessing optimal measurement parameters by analyzing spectra acquired with different pulse sequence at specific echo-times, analyzing the spectra in LCModel and identifying the parameters with lowest CRLBs as the optimal method of measuring specific metabolites (*22, 23*) .

The issue with identifying the optimal parameters from studying a subset of parameters is that the sampled subset might not consist of the optimal parameter. A more reliable study would be to include a full set of parameters to identify the set with the lowest CRLB i.e. the highest possible precision. While *in vivo* and *in vitro* studies with a complete sampling scheme are not feasible, calculations of theoretical CRLBs from composite spectra generated using simulated basis set are attainable. Considering the spin systems of metabolites of interest are widely available, generation of basis sets for different pulse sequence and a range of echo-times and calculating the theoretical CRLBs would be highly efficient in studying and maximizing the information content at different acquisition parameters.

A detailed method for calculating CRLBs and its implementation in calculating the optimal echo-time for detecting different metabolites using PRESS sequence at 7 Tesla is presented in Chapter 3.

CHAPTER III

OPTIMIZATION OF DETECTION PARAMETERS FOR METABOLITES AT 7 TESLA

3.1 Introduction

The detection and accurate quantification of brain metabolites *in vivo* by high resolution MR spectroscopy (MRS) continues to improve in parallel with increases in field strength, Larmor frequencies, and spectral resolution. Whereas a handful of methyl groups from abundant molecules such as N-acetylaspartate, creatine, and choline are routinely detectable at lower fields, the emergence of 7 Tesla instruments has made the measurement of less concentrated, coupled spin-systems, notably GABA and glutamate, more feasible. However, the transition to higher field also introduces new technical challenges, primarily because of constraints on current RF hardware, pulse designs, specific absorption rate (SAR) and field (B1 and B0) uniformities. At 7 Tesla the radiofrequency wavelengths approach the dimensions of human brains and add to the difficulty in optimizing experimental protocols and RF waveforms and realizing the full benefit of moving to 7 Tesla.

During such a period of evolution, previously tested and familiar protocols, whose precision and robustness are well established at lower fields, must be updated. Increases in the available spectral resolution and sensitivity dictate that rigorous approaches for assessing the effects of sequence parameters be developed. For example, spectral editing is more important at lower fields as a strategy to counteract lower inherent resolution whereas the necessary RF bandwidths and relaxation rates increase at higher fields.

Methods that objectively quantify the precision of measurements can be used to provide useful guidance on the selection of methods and experimental parameters.

One approach is to estimate the theoretical precision of detecting and quantifying specific metabolite time-domain signals against a background of other known metabolite signals (*24*). Using Monte-Carlo methods, the precision is determined by the convergence of standard errors in linear regression fits in the presence of randomly varying noise. For an unbiased estimator, these errors converge to the Cramer-Rao lower bounds (CRLBs) at a fraction of the computational cost. CRLBs therefore offer a direct and rapid method of comparing the impact of experimental variables on the nominal precision of metabolite measurements (*25, 26*).

Measurement precision has been previously evaluated for subsets of available field strengths, commonly measured metabolites, and various pulse sequence parameters. However, comprehensive assessments of metabolite precision and their variations with echo-time and resolution at 7 Tesla have not been reported. Hancu et al. acquired *in vivo* data on a 3 Tesla system at five echo-times (15, 35, 45, 80 and 144 ms) and evaluated the relative precision based on CRLBs obtained from LCModel (*19, 22*). By comparing spectral overlap between 2.3 -2.45 ppm, Snyder et al. determined that the optimal echo-time for Glu and Gln is 109 ms at 7 Tesla. Along with these studies, a basis for the theoretical bounds on precision for practical MR pulse sequences across a range of acquisition parameters would be valuable for developing high field detection strategies.

We have calculated CRLBs for 17 human brain metabolites that are at or near the detection threshold as a function of echo-time and resolution in PRESS. This analysis was extended to include projected 2-d acquisitions (TE-averaged) with all permutations

of uniform echo-time spacing. We anticipate that these results will be useful as a guide for estimating nominal precision of metabolite measurements at 7 Tesla.

3.2 Methods

3.2.1 Spectral Simulation

Basis spectra were calculated using programs written in C++ with the GAMMA libraries (*27*), as previously described (*11*). Seventeen metabolites were chosen to represent the most concentrated brain metabolites, and although some are currently undetectable, these compounds contribute to the theoretical precision of their more abundant counterparts and are therefore included in the analysis. Spin-systems were taken from Govindaraju (*15*) and density matrices were propagated in 1 ms increments over echo-times ranging from 30 to 180 ms by varying the second refocusing period in PRESS (*28*). Simulated metabolite concentrations for 10 of the 17 metabolites are shown in Table 3.1 (complete set with CRLBs in Appendix B.1). Spectra were normalized by incorporating within each spin-system a singlet reference peak well outside the bandwidth of interest (15 ppm).

Met	Cre	GABA	Gln	Glu	Gsh	mI	NAA	NAAG	PCh	sI
[C]	8.0	1.5	4.5	10.0	2.0	6.5	15.0	2.0	2.0	0.5

Table 3.1. Metabolite concentrations used in simulations.

3.2.2 Statistics

CRLBs (*20, 29*) were calculated with the expression given in Cavassila et al (*24*). Measured *in vivo* spectra $Y(v_k)$ at frequency v_k were modeled as:

$$Y(v_k) = X(v_k) + e(v_k) \tag{3.1}$$

and

$$X(v_k) = \sum_{l=1}^{N} C_l M_l(v_k) \tag{3.2}$$

where M_l are the simulated basis set spectra, C_l is the concentration of metabolite *l*, and $e(v_k)$ represents Gaussian white noise with a standard deviation σ^2. $Y(v_k)$, $M_l(v_k)$ and $e(v_k)$ are complex numbers with the assumption that the standard deviation of the real and the imaginary parts of the noise are equal. This model can be cast in matrix form as follows:

$$Y = M^T C + e \tag{3.3}$$

The general method to calculate CRLBs requires inverting the Fisher information matrix F, where

$$F = E\left[\left(\frac{dX}{dC}\right)^T\left(\frac{dX}{dC}\right)\right] \tag{3.4}$$

and E stands for the expectation. In the context of this study, F simplifies to

$$F = \frac{Re(M^H M)}{\sigma^2} \tag{3.5}$$

Here M is a N x 17 matrix which contains $M_l(v_k)$ as columns, M^H denotes the Hermitian conjugate of M, and R stands for the real part. Finally, the CRLBs are obtained as the square roots of the diagonal entries of the inverse of F:

$$CRLBs = diag\left(\sqrt{\left(F^{-1}\right)}\right) \quad (3.6)$$

CRLB calculations were first validated by comparison to Monte Carlo simulations, where experimental cut-off was chosen based on convergence of NAA standard deviations to 0.01% (number of repetitions, n = 4000*)*. The magnitude of the Gaussian distributed noise was adjusted to match the signal-to-noise achieved in *in vivo* spectra with respect to NAA data averaged over 8 minutes from a 40 x 30 x 15 mm^3 voxel at 7 Tesla on a Philips Achieva human scanner (Philips Healthcare, Best, The Netherlands). Metabolite bases were broadened to match *in vivo* Cre linewidths (3.03 ppm resonance, linewidth = 10.3 hz). For extension to a range of transverse relaxation times, CRLBs were modeled for T2 = 109 ms and T2 = 158 ms. These values correspond to reported T2s for Cre (109 ms) and NAA (158 ms) at 7 Tesla (*30*). The standard deviation of individual fits mirrored the calculated CRLBs, in accord with theory. Monte Carlo simulations were also used to interrogate cases where 2-hydroxyglutarate was: i) included in the composite spectra and in the basis set, ii) included in the composite spectra but not in the basis set, and iii) included in the basis but not in the composite spectra.

3.2.3 *In vivo* experiments.

For comparison to simulated bases at calculated extrema, i*n vivo* data were acquired at 7 Tesla on a Philips Achieva human scanner from 40 x 30 x 15 mm^3 voxels placed in the anterior cingulate cortex of two healthy volunteers, scanned in accordance with a protocol approved by the Vanderbilt University Institutional Review Board. 128 single echo transients localized with PRESS were acquired with TE/TR = 109/4000 ms.

Individual free-induction decays were frequency and phase corrected prior to averaging using a previously reported post-processing algorithm (*4*)

3.3 Results and Discussion

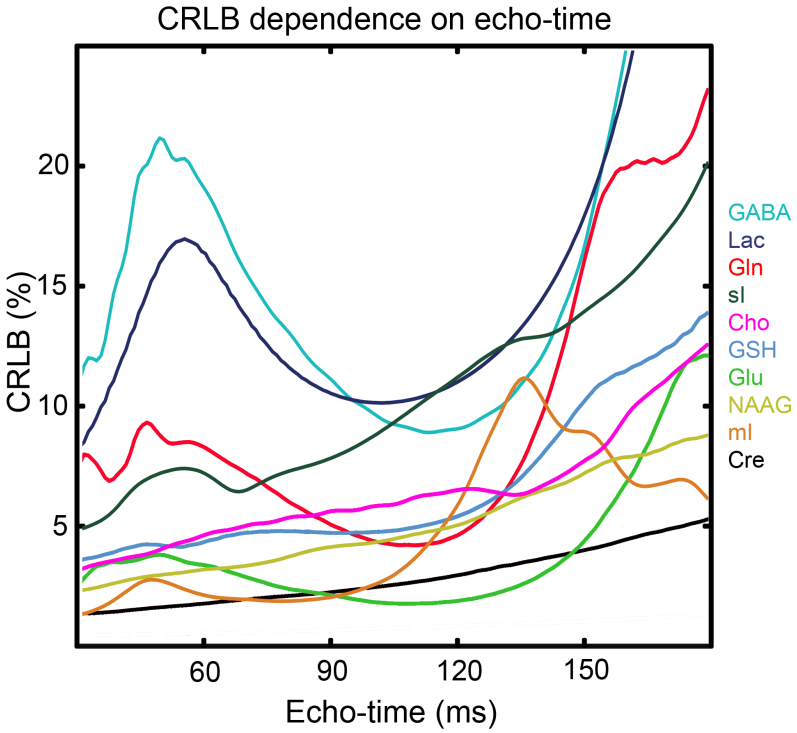

Figure 3.1. Dependence of metabolite lower bounds of precision (CRLBs) on echo-time for T_2 = 109 ms.

TE	Cre	GABA	Gln	Glu	Gsh	mI	NAA	NAAG	PCh	sI
T2 = 109 ms										
30	1.2	11.1	7.6	2.5	3.5	1.2	0.3	2.2	3.1	4.8
109	2.6	9.1	4.1	1.7	4.9	3.4	0.7	4.6	6.1	9.8
T2 = 158 ms										
30	1.1	10.2	7.0	2.3	3.2	1.1	0.3	2.0	2.8	4.4
110	1.9	6.6	3.0	1.2	3.6	2.6	0.5	3.4	4.5	7.3

Table 3.2 CLRBs for PRESS acquisitions at 30 and 109 ms between T2 bounds of 109 and 158 ms.

3.3.1 CRLB trends with echo-time

Figure 3.1 shows theoretical CRLBs as a function of echo-time for 10 of the 17 metabolites used in this study. The full set of CRLB curves is included in Appendix B2. There are three distinct trends in metabolite Cramer-Rao Lower Bounds (CRLBs) in PRESS sequence over the echo-time range from 30 to 180 ms (Figure 3.1). Nominal precision decreases with echo-time from 30 ms to a minimum (CRLB peak) for most metabolites at approximately 50 ms in the first major trend. This trend begins at 0 ms, but echo-times less than 30 ms were excluded from further analysis because they are not practical at 7 Tesla with this sequence.

Progressing to higher echo-times, in the second major trend methylene spin-systems (e.g. AA'XX') begin to refocus. Relative to the global minimum for all metabolites at TE = 0 ms, a secondary trough develops at ~ 110 ms which is most pronounced for GABA, Lac, Glu and Gln (Figure 3.1). Two distinct peaks for Glu and Gln are visible at 109 ms and coupled with minima for CRLB allows simultaneous detection of Glu and Gln (Table 3.2, Figure 3.2). A spectrum obtained *in vivo* at an echo time of 109 ms is shown in Figure 3.2. This finding agrees with the optimal PRESS echo-time previously reported by Snyder et al (*31*).

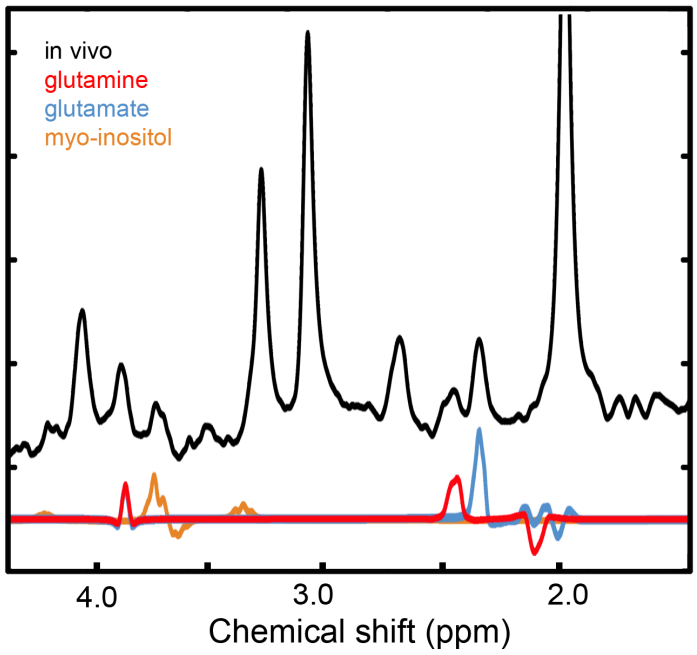

Figure 3.2. *In vivo* spectrum shown with 3 spectral bases (glutamine, glutamate, inositol) at the echo time optimum for Gln and Glu (109 ms) at 7 Tesla.

Beyond this CRLB trough at 110 ms, precision uniformly decreases in the third trend as CRLBs are dominated by coupled spin modulation with an added effect from T2 dephasing. We observe increasingly heavy penalties for attempting metabolite measurements with PRESS at echo-times greater than 110 ms.

3.3.2 CRLB vary with molecular structure

The dominant trends shown in Figure 3.1 can be further subdivided by molecular structure. The set of detectable *in vivo* metabolites can be roughly divided into 4 groups: 1) amino acids (Glu, Gln and GABA), 2) molecules with uncoupled methyl groups (NAA, Cre, Cho), 3) carbohydrates (mI and stereoisomer sI), and 4) peptides (NAAG and GSH). Molecules with coupled methyl protons such as Lac and Ala exhibit harsh

penalties progressing from TE = 0 to 50 ms and deep oscillations at echo times greater than 100 ms.

Uncoupled methyl protons contain intense absorptive resonances that do not modulate as a function of echo-time. The corresponding dependence of CRLBs on echo-time reflects this – the precision of NAA, Cre, and Cho decrease monotonically with T2 relaxation. These molecules also feature the lowest CRLBs overall, and can be measured with high precision across the range of 30-110 ms considered here. Amino acids on the other hand, are also of broad interest and require more careful planning for optimal measurement efficiency.

Amino acids present in brain tissue and detectable by ^{1}H MRS include the major inhibitory neurotransmitter (GABA), the major excitatory neurotransmitter and metabolic intermediate (Glu), as well as the most abundant amino acid in circulation (Gln). At typical *in vivo* concentrations (*11*), GABA is not detectable with a CRLB less than 10% with PRESS at 7 Tesla at any echo-time with the SNR considered in these calculations. Even at 7 Tesla, spectral editing or 2-dimensional methods are therefore required to measure GABA. Glu and Gln are more concentrated, and Glu in particular is sufficiently abundant to be detected either at short echo-times near 30 ms or at the global minimum (109 ms, for echo-times > 30 ms). At approximately half the concentration of Glu, Gln will likely be difficult to detect at echo-times other than the optimal (110 ms at T2 = 109 ms). This agrees with a recent study by Snyder et al, which showed that minimum overlap for Glu and Gln was near 110 ms and independent of the way the individual echoes were distributed (*31*).

These results are also consistent with analyses that focused only on the 2.2 – 2.6 ppm range for Glu and Gln and that support an echo time of 110 ms (*32, 33*). Our results are in excellent agreement with these studies despite the use of different analysis methods. Downfield resonances at 3.75 ppm are of limited value for Glu and Gln quantification because their chemical shifts and J-couplings are nearly identical; they act only to constrain the model in the more upfield region that is characterized by mutually exclusive information content.

The third major set of components of human brain spectra considered here are inositol compounds. These are synthesized from glucose and of the 8 isomers, mI and to a lesser extent sI are present in sufficient abundance to be detected in human brain. Methyl groups and amino acids demonstrate monotonic increases and global minima near 110 ms, respectively, and, in contrast, the CRLBs in mI and sI display shallow minima at 70 ms before losing precision at higher echo-times (Figure 3.1). Given this behavior, the amino acids and inositol compounds cannot be simultaneously measured with optimal precision at a fixed echo-time.

The final classes of compounds considered here are peptides. NAAG and Gsh are di and tripeptides, respectively, and feature CRLB trends that are distinct from the other compounds presented above. In both cases, the trends most resemble the monotonic increases seen in methyl-bearing molecules, suggesting that the added J-coupled resonances add negligible spectral information. In contrast to Glu and Gln for example, the CRLBs of GSH and NAAG exhibit very shallow minima in measurement precision beyond 50 ms.

3.3.3 CRLB dependence on linewidth.

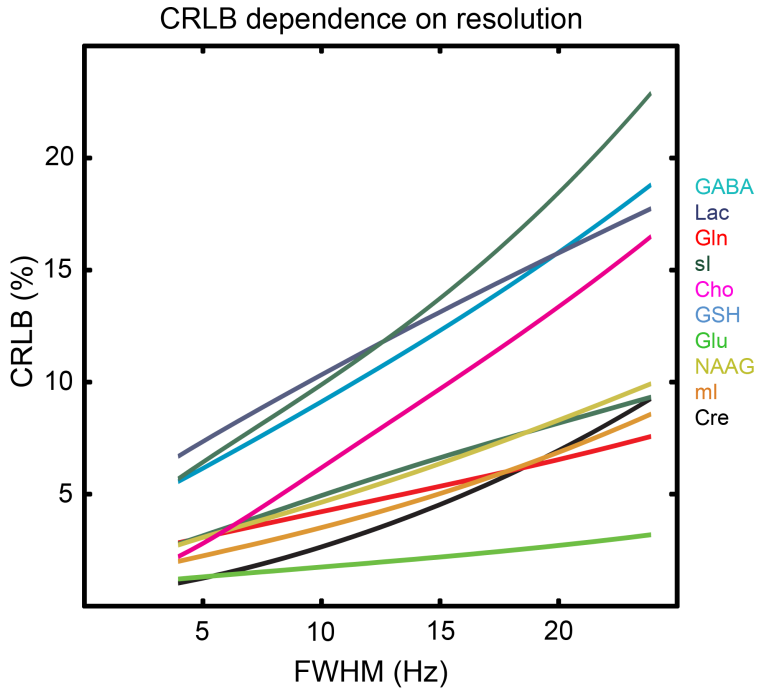

Figure 3.3 Dependence of metabolite lower bounds of precision (CRLB) on resolution for T_2 = 109 ms 4 to 24 Hz.

	Cre	GABA	Gln	Glu	Gsh	mI	Lac	NAA	NAAG	PCh	sI
a	0.41	0.66	0.24	0.10	0.33	0.33	0.55	0.05	0.36	0.72	0.85
b	1.50	2.32	1.71	0.67	1.41	0.15	4.49	0.11	0.91	-1.27	1.28
r2	0.98	1.00	1.00	1.00	1.00	0.99	1.00	1.00	1.00	1.00	0.99

Table 3.3. Linear (y = ax + b) fit of CRLB (y) versus linewidth (x) centered at TE = 109 ms.

The dependences of CRLBs on linewidth are shown in Figure 3.3. These are estimated for TE = 109 ms and displayed in Hz. Linear slopes (CRLB/Hz, Table 3.3) range from 0.05 (NAA) to 0.85 (sI) with minimum and maximum intercepts at 4 Hz ranging from

0.37 for NAA to 6.63 for Lac. The intercepts depend on concentration (Table 3.1). For the concentrations used in this study, the CRLB for Glu is relatively insensitive to linewidth near the optimal echo-time. However, as echo-times move away from this trough, resolution must increase to maintain a constant CRLB. This can be seen from the isolines plotted against linewidth (FWHM) and echo-time in Figure 3.4.

3.3.4 Strategies for simultaneous detection of inositol compounds and amino acids.

The CRLB contours for Gln are similar to Glu in Figure 3.4 and, in both cases, measurement precision becomes increasingly less sensitive to linewidth when echo-times move from 45 toward 110 ms (Figure 3.4). Contrasting with the CRLB surfaces of these 2 amino acids, mI and sI require increasing resolution to maintain constant precision with echo-times greater than 95 ms. These CRLB contour plots preclude simultaneous detection of Glu, Gln and mI and sI at one echo time.

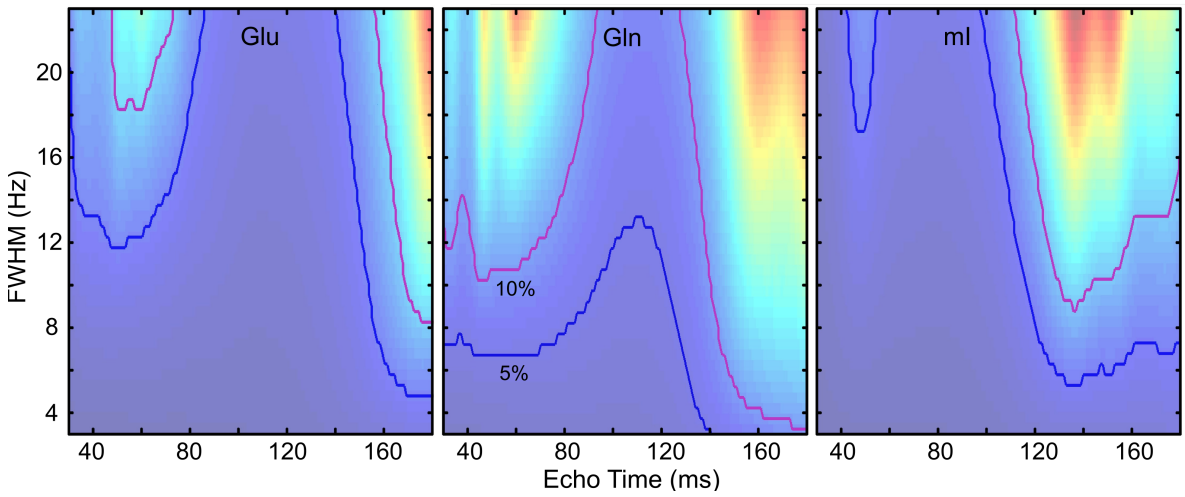

Figure 3.4. CRLBs of glutamate (left), glutamine (center), and inositol (right) as a function of resolution (FWHM) and echo time at a proton frequency of 300 MHz (7 Tesla). Isolines for 5 and 10% CRLB are shown in blue and purple.

At the transverse relaxation rates used in these calculations (109 ms and 158 ms) (*30*), Glu and Gln are detected with maximum precision at ~110 ms (109 ms for Glu), while measurement of mI is most favorable at 30 ms and the secondary CRLB trough at 78 ms. The CRLB for Glu and Gln increases from 1.7 and 4.1 at 109 ms to 2.4 and 6.2 at 78 ms, respectively. The CRLB for mI increases from 1.8 at 78 ms to 3.4 at 109 ms. The optimal measurement strategies for this metabolite subset depend on how much precision can be sacrificed for either compound of interest (Glu/Gln versus mI). Single echoes may be chosen for individual measurements, but the most efficient use of spectrometer time would divide attention between the respective metabolite optima in paired echo averages.

Sequences which average echo acquisitions with linearly increasing echo-times are referred to as TE-averaging (*34*). While research groups have found value in averaging echo-times in the range of 35-185 ms at 3 Tesla, these sequences are found to be less appropriate for a range of metabolites including Glu and Gln at 7 Tesla when considering CRLBs in the model used here. Adding echoes reduces precision for a given metabolite relative to its CRLB minimum, but the practice is useful for making efficient use of spectrometer time when the objective is to make measurements with optimal precision in sets of metabolites. Under these conditions, combining echo-times in a single scan eliminates the necessity of starting and restarting the acquisition, while reducing the number of data sets for post-processing and analysis by 50 percent.

3.3.5 CRLBs with TE-averaging schemes

Figure 3.1 illustrates how precision of measurement varies for each of 10 metabolites against a background of Gaussian distributed noise. For any single metabolite, averaging echoes away from the optimum value reduces precision. The rate that penalties in precision accrue depends on the sharpness of the CRLB minima for each metabolite. For any pair of metabolites of interest, averaging echoes will be less precise for each compound.

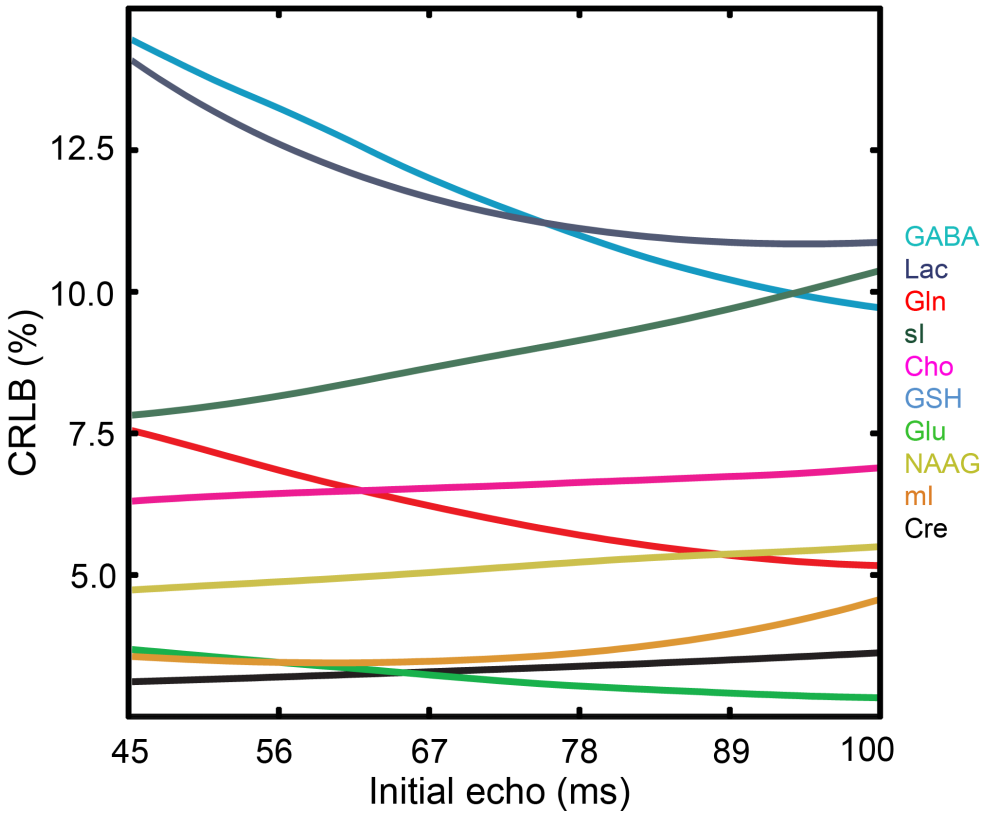

Figure 3.5. Metabolite CRLBs in projected 2-d sequences. These curves represent the CRLB of echo-time averages where the starting echo series ranges from 45 to 100 ms in 1 ms increments. For example, the first point includes the CRLB from echoes over the range from 45-100 ms, whereas the last point spans 100-120 ms.

Cre	GABA	Gln	Glu	Gsh	mI	NAA	NAAG	PCh	sI
Signal average of 30 and 109 ms									
1.7	11.3	6.1	2.1	4.4	2.0	0.4	3.0	4.7	6.2
Signal average of 35 and 118									
1.8	11.6	7.0	2.8	4.8	2.6	0.5	3.2	5.1	6.6
Signal average of 78 and 109									
2.2	11.7	5.4	2.1	4.8	2.4	0.6	4.1	5.7	8.1
35 to 185 ms in 10 ms increments									
2.4	17.8	10.9	3.7	6.0	4.1	0.6	4.5	6.9	8.8

Table 3.4. CRLBs for echo averaging schemes with T2 at 109 ms.

A snapshot of the performance of averaging schemes is illustrated in Figure 3.5. The ordinate in this figure represents the starting average in uniformly sampled data ranging from 45 to 100 ms. Hence, increasing initial echo-time corresponds to fewer echoes averaged along with a concomitant bias to higher echo-times. The amino acids and Lac benefit from this bias and CRLBs can be seen to converge to their respective single echo minima, while other metabolites (with more favorable CRLBs at lower echo-times) become increasingly worse.

The trade-offs involved in projecting (averaging) echoes can be seen from Figure 3.1 and the prior discussion of CRLB trends as a function of echo-time and molecular structure. Amino acids such as Glu and Gln feature large CRLB oscillations with primary troughs at ~109 and 30 ms. Stereoisomers of inositol, such as mI and sI, have primary and secondary troughs at 30 and 78 ms, respectively. The measurement precision of both amino acids and inositols are heavily penalized at CRLBs near 50 ms. Methyl-bearing

molecules are driven by T2 losses and CRLBs increase monotonically across the range of analysis considered here (30-300 ms). While single echoes at respective optimum echo-times outperform projected sequences uniformly, when inositols and amino acids are of interest, combining 30 and 109 ms or 78 and 109 ms would be expected to provide the best compromise and reduce scan-time. According to our simulations, 30 and 109 ms should outperform other averaging schemes and lead to the most efficient use of scan time for detection of all three major subdivisions considered here (Table 3.4). To the extent that other metabolites are of interest and not included (such as Lac), modifications will be necessary but optimal conditions are straightforward extensions of the analysis presented here.

3.3.6 Basis set composition

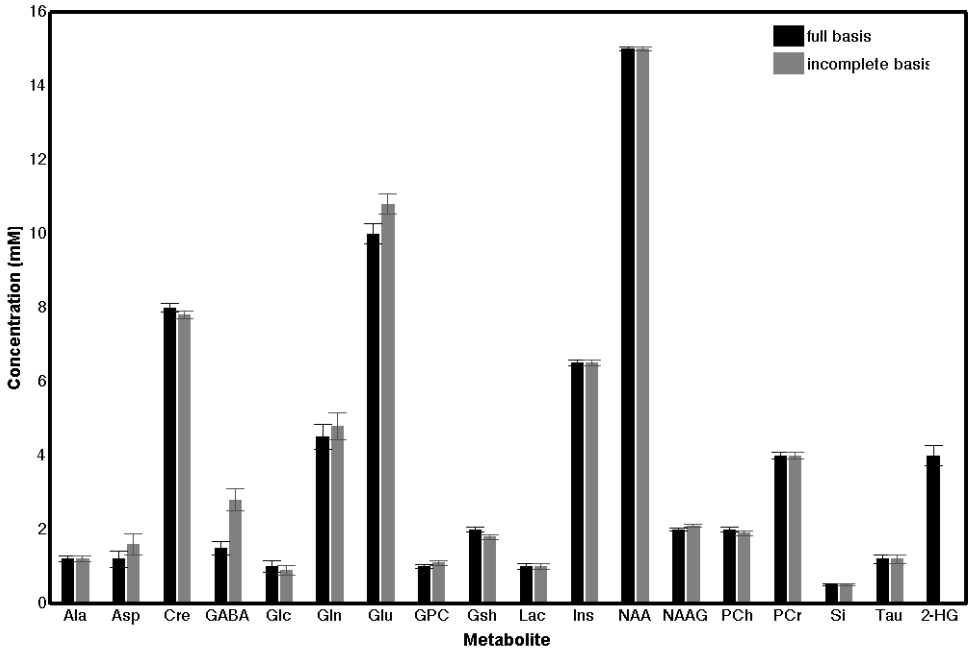

Figure 3.6. The dependence of concentration on basis set composition. When 2-hydroxyglutarate is physically present but not used in the fitting for quantification, the concentration of glutamate, glutamine, and γ-aminobutyric acid are overestimated (gray trace) relative to input concentrations (black trace).

Figure 3.6 shows the results from quantification of metabolites, concentration and associated CRLBs from a system of 18 metabolites that include 2-hg in addition to the 17 metabolites discussed above. The two cases shown are: i) inclusion of 18 metabolites in both the composite spectrum and the basis set, and ii) exclusion 2-hg in the basis set but inclusion in the composite spectrum generated from 18 metabolites. Monte-Carlo simulation results show agreement between CRLBs from cases i) and iii) , whereas case ii) shows overestimation of concentrations of Glu, Gln, GABA and Asp. For example, addition of 4 mM of 2-HG in the composite spectra and absence in the spectral basis set resulted in the output concentration of glutamate, glutamine and GABA to be estimated as 10.8, 4.8 and 2.8 mM when there was only 10, 4.5 and 1.5 mM of these metabolites in the composite set respectively as can be see from Figure 3.6. However, this overestimation of concentration is not reflected in the metabolite precision from these experiments. This suggests that excluding metabolites in the basis set that are present in the experimental data leads to an error in concentration estimates without the information being reflected in error estimates.

3.4 Conclusions

Metabolite precision as a function of echo-time was studied at 7 Tesla at resolutions typical for human brain. Theoretical Cramer-Rao lower bounds (CRLBs) were used to determine nominal measurement precision for 17 metabolites in order to tailor optimal detection strategies for PRESS and TE-averaged acquisitions. Standard deviations from Monte Carlo simulations converged to CRLBs for subsets of the echo-times analyzed,

validating the previously reported algorithm (*24*). Whereas the relationship between CRLBs or Monte Carlo and *in vivo* data depend on prior knowledge of the model, and in particular the baseline and noise, the trends with echo-time are likely dominated by chemical shift and J-modulation.

The theoretical CRLBs of human brain metabolite spectra as a function of echo-time in PRESS suggest that trends in precision are dominated by structural motif. This occurs despite a range of J-couplings because CRLBs are driven by evolution against the evolution of background metabolites. For example, the chemical shifts and J-couplings in glutamine and glutamate are similar, yet display a detection optimum within a millisecond (109 versus 110 ms). Using these overall trends, the detectable metabolites can be approximately subdivided into 4 classes (excluding lactate).

Optimal precision of amino acids and carbohydrates is mutually exclusive in the range of echo-times studied here (30 ms to 180 ms). When molecules from these classes are targeted, the required precision should be balanced with approximate concentrations and echo-times weighted accordingly. TE-averaged data can be acquired with standard scanners, and the use of multiple echoes in PRESS has been previously explored for measuring glutamate (*34*). While additional factors could make these strategies advantageous, analysis of the CRLBs suggests that the number of sampled echoes should equal the number of mutually exclusive molecular classes being examined. For example, when carbohydrates and amino acids are of interest, an efficient sampling scheme simply toggles between the respective optima. This solution consolidates both acquisition and analysis while maintaining optimal overall precision on a pair of metabolites where CRLB minima do not overlap.

We found that missing metabolites in the basis set that are present in the experimental data leads to overestimation of other metabolites, having a complete basis set that includes metabolites, like 2-hg, that might only be present in patients with IDH-2 mutations, does not reduce the accuracy of the metabolite quantification.

CHAPTER IV

IMPLEMENTATION AND COMPARISON OF GABA MEASUREMENTS AT 3 TESLA AND 7 TESLA

4.1 Introduction

GABA is a major inhibitory neurotransmitter and abnormal levels of GABA are associated with various neuropsychiatric disorders. For example, lower levels of GABA have been observed in patients suffering from depression and schizophrenia (*35, 36*). However, measurements of GABA are difficult because the concentration is low (around 1 mM), which is at the detection threshold of MRS measurements in reasonable times. Moreover, there is significant spectral overlap from resonances from methyl groups like NAA and Creatine that have concentrations that are at least four times that of GABA, so spectral editing techniques are essential to select and quantify GABA in vivo. Various methods have been proposed and used, and among these different spectral editing techniques, one of the widely used sequence is J-difference editing, which is performed by employing the MEGA-PRESS sequence (*3*). The pulse sequence diagram for the MEGA-PRESS pulse sequence is shown in figure 4.1.

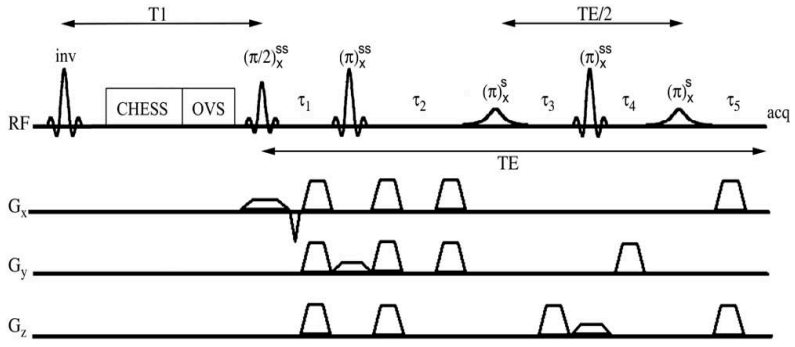

(Waddell et al 2007)

Figure 4.1. MEGA-PRESS J-difference editing pulse sequences.

With the advent of increased field strength and accompanying SNR, the development of specialized pulse sequences and advances in data correction and analysis techniques, there is increased interest in measuring GABA despite the previous difficulties to detect it reliably (*37, 38*). In particular, the emergence and wider use of 7 Tesla MR scanners brings with it the potential for acquiring data with higher signal-to-noise ratio and better spectral resolution. Moving to a different static magnetic field strength affects some of the metabolites MR properties such as T1 and T2 relaxation times as well as chemical shift dispersion, which imposes the demand for proportionately larger RF excitation bandwidths. Longer T1 relaxation times requires longer repetition times to allow recovery of the magnetization, which lengthens the duration of the scan while shorter T2 relaxation times result in faster signal decay and broader lines and signal bandwidths as we go to higher field strength.

One of the factors that potentially affects the measured concentration of GABA is contamination from macromolecular resonances that are known to co-edit with GABA with most GABA editing sequences (*39-41*). Macromolecules usually have shorter T2 relaxation times and hence we would expect to have decreased contamination from macromolecules at 7 Tesla compared to 3 Tesla. However, the assessment of the differences in the degree of contamination from macromolecule is beyond the scope of this study and is not considered here.

Here, we compare the performances and results of measuring GABA in human brain using both 3T and 7T systems. We report on measured differences between the neurotransmitter concentrations observed between 3 Tesla and 7 Tesla and assess the bandwidth requirements for making metabolite measurements with higher precision at 7

Tesla. We believe these results will be helpful in identifying the parameters necessary for increasing the quantification accuracy of GABA and improve the measurements at 7 Tesla.

4.2 Methods

15 volunteers were scanned for this study using protocols approved by the Vanderbilt University Institutional Review Board. All scans were performed on 3 Tesla and 7 Tesla Philips Achieva MR Scanners (Philips Healthcare, Best, The Netherlands). A birdcage transmit/receive head coil was used for 3 Tesla experiments and a volume transmit head coil (Nova Medical, Inc, Burlington, MA, USA) in combination with a 16-channel receive coil (Nova Medical, Inc, Burlington, MA, USA) was used for 7 Tesla experiments.

4.2.1 Imaging

Anatomical images were acquired using T1-weighted turbo field echo (TFE) sequence with 1x1x2 mm^3 resolution, TE/TR = 3.19/6.54 ms, field-of-view (FOV) size of 240x240x170 mm^3, number of slices = 85 with 64x63 pixels, water-fat shift = 2.02 pixels for a scan time of 5 minutes. All anatomical images were acquired in sagittal planes and reformatted to generate axial and coronal planes for accurate voxel placements.

4.2.2 Spectroscopy

All spectroscopy data were acquired from a 40x30x15 mm^3 voxel in the anterior cingulate cortex (ACC). The data were first acquired at 7 Tesla and the voxel at 3 Tesla

was specified to match the voxel used for 7 Tesla measurements using screen grabs of voxel location in all three planes from 7 Tesla as reference for each subject.

3 Tesla vs 7 Tesla measurements

11 subjects were first scanned at 7 Tesla and then at 3 Tesla with the voxel location matched to the one used at 7 Tesla. At 3 Tesla, 512 transients were acquired with a transmit/receive birdcage coil with a maximum B1 of 23.5 μT. The data were acquired using MEGA-PRESS sequence with TE/TR = 73/2000 ms with 2048 points in the FID, 2 kHz receiver bandwidth. The frequency selective pulses had a bandwidth of 64 Hz for GABA editing and were alternated between 1.9 ppm on odd acquisitions and at 7.4 ppm on even acquisitions. Four outer volume suppression bands and a sinc-gauss pulse with 130 Hz bandwidth for water suppression were applied before the MEGA-PRESS pulse sequence and the slice-selective pulses were centered on 2.02 ppm.

At 7 Tesla, 256 transients were acquired with a volume transmit/receive coil with a maximum B1 of 15 μT and the 16 channel SENSE coil as the receive coil. The data were acquired using a MEGA-PRESS sequence with TE/TR = 73/4000 ms with 2048 points in the FID, 3.5 kHz received bandwidth. The frequency selective pulses had a bandwidth of 149 Hz for GABA editing and were alternated between 1.9 ppm on odd acquisitions and at 7.4 ppm on even acquisitions. MOIST water suppression with a bandwidth of 150 Hz along with four outer volume suppression bands was applied prior to the localization pulse sequence and the slice-selective pulses were centered on 2.02 ppm.

Bandwidth effect at 7 Tesla

Three sets of GABA edited spectra were acquired from the same voxel location with the RF pulse centered on NAA at 2.02 ppm from 4 volunteers. The manufacturer set maximum B1 was overridden from 15 μT to 18 μT. Three sets of data were acquired by applying RF pulses with maximum B1 of 15 μT, 16.5 μT and 18 μT to study the effect of pulse bandwidth at 7 Tesla. The slice-selective excitation and refocusing pulses used in this study and their corresponding pulse profiles are given in Figure 4.1. The bandwidths of the excitation pulses and the refocusing pulses at different RF amplitude are given in Table 4.1.

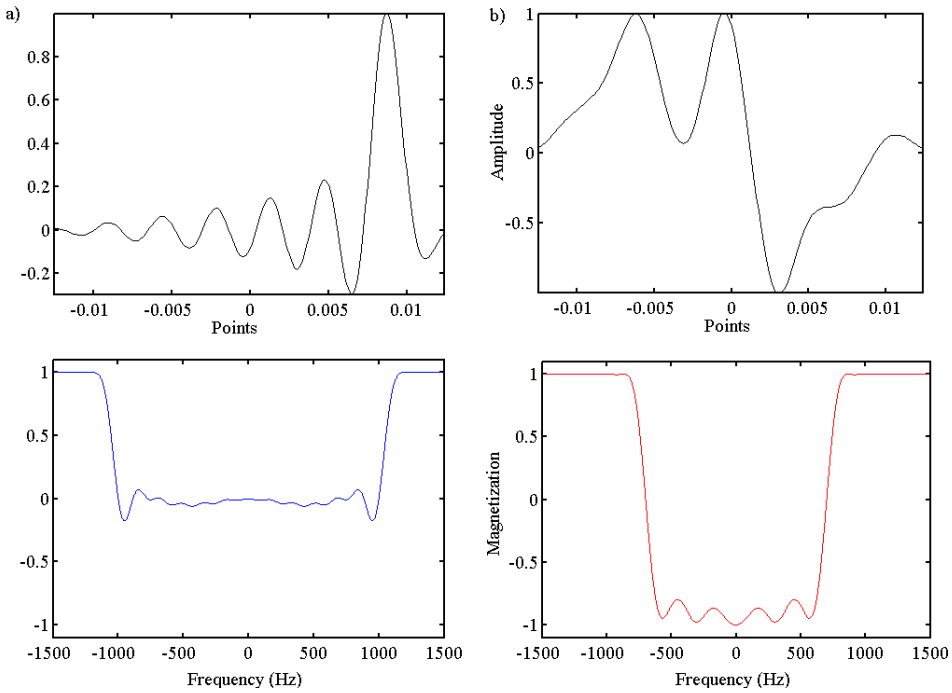

Figure 4.2. Pulse profile (top) and frequency response (bottom) for a) excitation pulse and b) refocusing pulse used in the study.

	Excitation pulse spredrex		Refocusing pulse gtst1203	
B1 (uT)	Time (ms)	BW (Hz)	Time (ms)	BW (Hz)
15	6.41	2210	6.22	1405
16.5	5.83	2431	5.65	1546
18	5.34	2652	5.18	1686
23.5	4.09	3463	3.97	2202

Table 4.1. RF amplitude (B1), corresponding pulse duration and pulse bandwidth (BW) of the excitation (spredrex) and refocusing (gtst1203) pulses used in the study.

4.2.3 Post-processing

All datasets were zero filled to 8192 points and line broadened with a 2 Hz frequency and phase-corrected using programs written in Matlab using the 3.03 ppm singlet peak from Creatine as reference. After the frequency and phase corrections, the even acquisitions were averaged into an even spectrum and the odd acquisitions into an odd spectrum. The even spectrum was subtracted from the odd spectrum to generate the J-difference spectrum.

4.2.4 Analysis

Full density matrix simulations were performed for PRESS and MEGA-PRESS sequences using ideal pulses as slice-selective pulses and real pulses as frequency-selective editing pulses (in MEGA-PRESS) using programs written in C++ by incorporating GAMMA subroutines (*17*). The density matrices for the MEGA-PRESS sequence were sampled from 10^4 spatially resolved points within the voxel to account for

the differential impact of crusher gradients in the presence of spectrally selective editing pulses. The spin system were taken from the literature, the resulting spectra were normalized and formatted for use as a basis set in LCModel (Chapter 2). Metabolite concentrations from even and J-difference spectra from all volunteers were quantified using LCModel (*19*).

4.2.5 Chemical shift displacement calculations

Slice-selective pulses have limited bandwidth and are applied in the presence of a magnetic field gradient in order to affect a specific target region of the sample resulting in a shift in the effective location of the selected slice for different resonances. This shift is given by:

$$\Delta x = \frac{\Delta\omega}{BW_{rf}} x \tag{4.1}$$

where x is the size of the voxel, $\Delta\omega$ is the difference in chemical shift between two protons, BW_{rf} is the bandwidth of the RF pulse, Δx is the chemical shift displacement in the voxel direction (*2*). Equation 4.1 was used to calculate the chemical shift displacement errors at 3 Tesla and 7 Tesla measurements and assess the bandwidth requirements of the RF pulses for the 7 Tesla measurements to be comparable to 3 Tesla measurements and also requirements to outperform 3 Tesla measurements.

Chemical shift displacement errors result in the spin system experiencing 4 different pulse sequences based on the location of the spins, with the spins experiencing: a) all 3 pulses of the PRESS sequence, b) the 90^{o} and first 180^{o} pulses, c) the 90^{o} and the second 180^{o} pulses, and d) only the 90^{o} pulse. The GABA spectra generated from the different cases have been previously reported by Edden et al (*42*). The signal detected from the

study is the sum of signals arising from all 4 regions and the result may therefore suffer from signal distortion.

4.3 Results and discussion

4.3.1 3T vs. 7T measurement

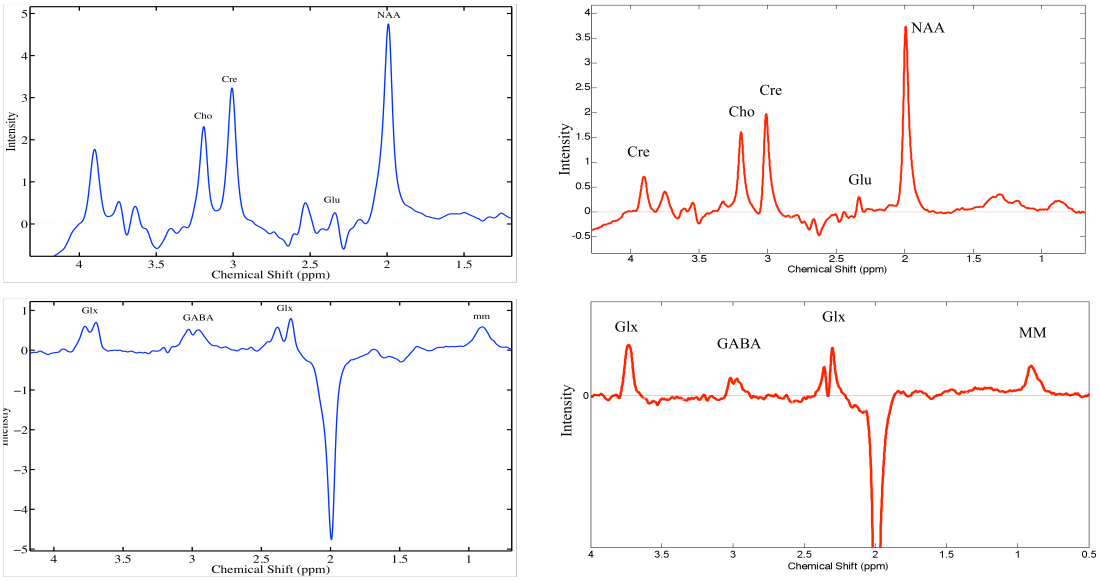

Figure 4.3. Even (top) and J-difference (bottom) spectra acquired at 3 Tesla (left) and 7 Tesla (right) using MEGA-PRESS sequence at TE = 73 ms with editing pulse bandwidth of 0.5 ppm toggled between 7.4 and 1.9 ppm on even and odd spectra respectively acquired from a 40x30X15 mm^3 voxel from anterior cingulated cortex.

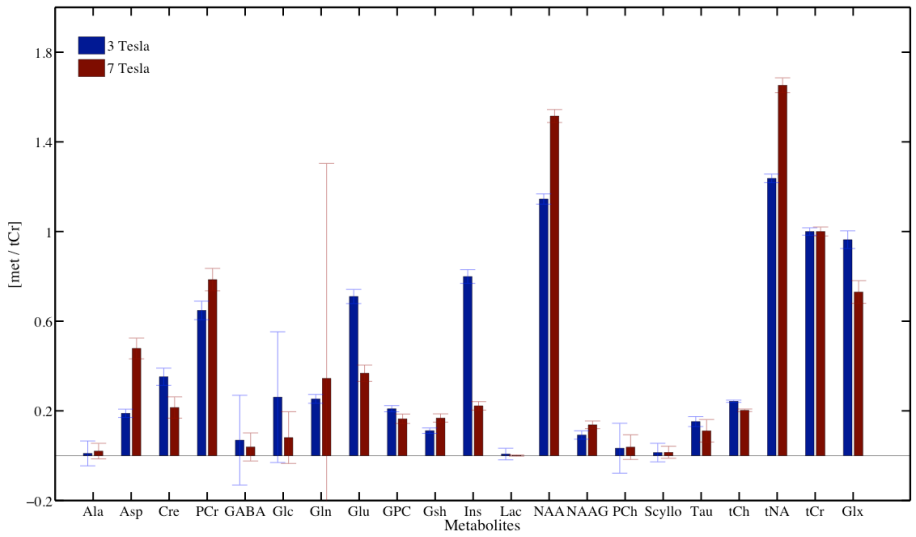

Figure 4.4. Comparison of metabolite-to-tCr ratios averaged from even analysis of 11 data sets acquired at 3 Tesla and 7 Tesla.

Figure 4.4 shows large discrepancies in [met]/[tCr] ratios between the even data acquired at 3 Tesla with B1 = 23.5 μT and 7 Tesla with B1 = 15 μT. The ratio of [NAA/tCr] was measured to be 1.65 at 7 Tesla vs 1.24 at 3 Tesla, [Glx/tCr] was 0.73 at 7 Tesla vs 0.96 at 3 Tesla and [Ins/tCr] was 0.22 at 7 Tesla vs 0.80 at 3 Tesla. The higher ratio of [NAA/tCr] at 7 Tesla denotes smaller peaks from Creatine measured at 7 Tesla than at 3 Tesla. As we move to metabolites that have resonances downfield from the center frequency of NAA (2.02 ppm) of the slice-selective pulses, the measured metabolite ratios get smaller at 7 Tesla in comparison to 3 Tesla.

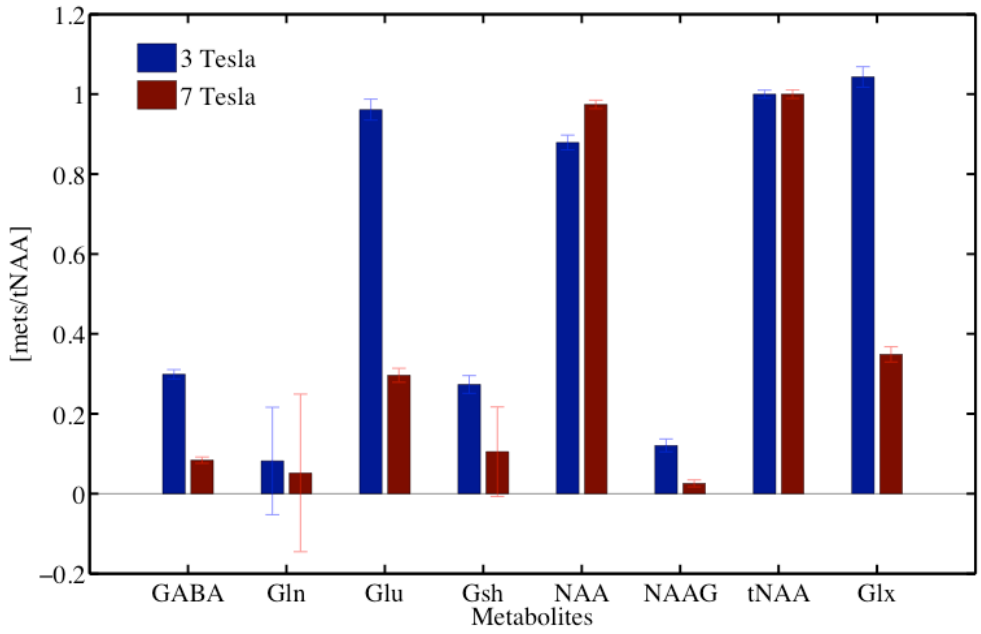

Figure 4.5. Comparison of metabolite-to-NAA ratios averaged from j-difference analysis of 11 data sets at 3 Tesla and 7 Tesla.

The results in Figure 4.5 from analysis of J-difference spectra show that [GABA/tNAA] measured at 7 Tesla was only 0.28 times the ratio measured at 3 Tesla and [Glx/tNAA] at 7 Tesla was 0.33 times that at 3 Tesla. The large discrepancy cannot be accounted for with the consideration of T2 relaxation rate differences and the decreased macromolecule contamination at 3 ppm for GABA measurement at 7 Tesla. The results make it apparent that the effects of chemical shift displacement errors with the maximum B1 of 15 μT used for 7 Tesla measurements are a setback to realizing the full benefit of moving to 7 Tesla from 3 Tesla and needs to be further analyzed.

4.3.2 Effect of RF and bandwidth at 7 Tesla

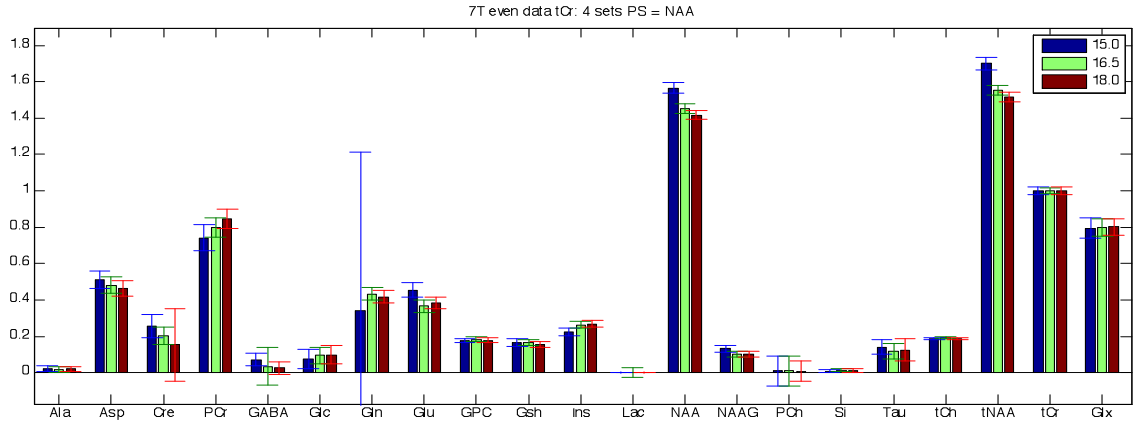

Figure 4.6. Comparison of metabolite-to-tCr ratios averaged from even analysis of 4 data sets acquired with RF amplitudes of 15, 16.5 and 18 μT.

Averages from analyses of 4 even data sets acquired from using three different B1 values, 15, 16.5 and 18 μT are shown in Figure 4.6. [tNAA/tCr] ratio decreases from 1.70 to 1.55 and 1.52 as the RF amplitude of the slice-selective pulses increase from 15 μT to 16.5 μT and 18 μT respectively. As the RF amplitude of slice-selective pulses increased from 15 μT to 16.5 μT to 18 μT, increases in ratios of [Glx/tCr] and [Ins/tCr] were also observed as is shown in Figure 4.6. Significant changes in [tCh/tCr] were not observed possibly due to the proximity of tCh and tCr resonances which are located at 3.2 ppm and 3.03 ppm respectively with a difference of 0.2 ppm.

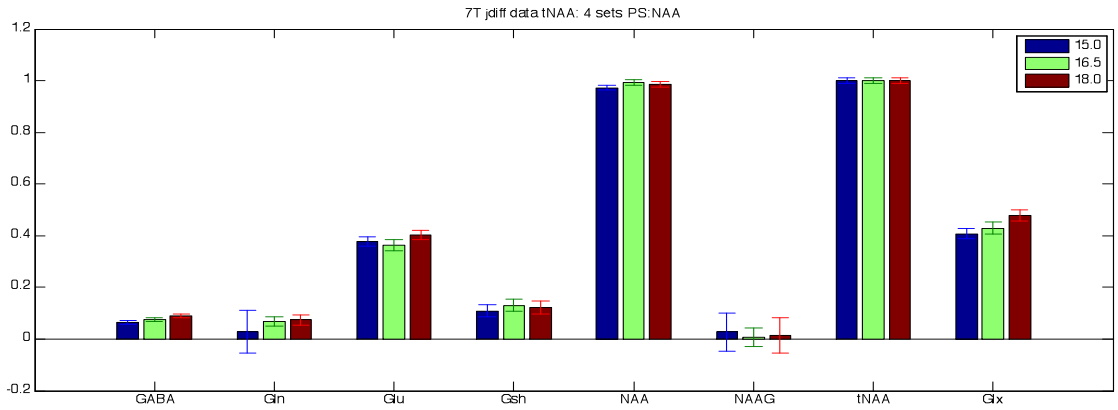

Figure 4.7. Comparison of metabolite-to-NAA ratios averaged from even analysis of 4 data sets acquired with RF amplitudes of 15, 16.5 and 18 μT.

Figure 4.7 shows averages of [met/tNAA] from J-difference analysis of data sets acquired with B1 values ranging from 15 μT to 18 μT. The figure shows increases in [GABA/tNAA] from 0.065 to 0.074 to 0.089 and [Glx/tNAA] from 0.407 to 0.430 to 0.478 with increases in B1 from 15 μT to 16.5 μT to 18 μT. Even though increasing the RF amplitude by 1.5 μT for the slice-selective refocusing pulses used in this study increased the bandwidth of the pulses by a mere 10%, the improvement in quantification accuracy is evident. All these results confirm the notion that a large proportion of the discrepancy in the results between measurement at 3 Tesla and 7 Tesla was due to the increase in chemical shift displacement errors at 7 Tesla because of decreased bandwidth of the pulses.

4.3.3 Chemical shift displacement errors

The extent of chemical shift displacement errors between 1.91 and 3.01 ppm resonances of GABA and between 2.1 and 3.7 ppm resonances of Glutamate for the RF amplitude and pulses used in this study are shown in Table 4.2. Table 4.2 shows a

chemical shift displacement error of 6.51 % and 9.53% between the resonances of GABA and of Glutamate respectively and displacements of 19% or more at 7 Tesla with the pulses used in this study with RF amplitudes of up to 18 μT. As the difference in chemical shift between two molecules or resonances increase, the chemical shift displacement errors also increase which results in incoherent averaging of the spectra generated from different compartments.

B0 field (T)	B1 (μT)	BW (Hz)	GABA (1.9-3.0ppm) % CS displacement	Glu (2.1-3.7 ppm) % CS displacement
7	15.0	1405	23.75	34.78
7	16.5	1546	21.59	31.61
7	18.0	1686	19.80	28.99
3	23.5	2202	6.51	9.53

Table 4.2. RF amplitudes, RF bandwidths and corresponding percent if chemical shift displacement errors in the voxel direction for a refocusing slice-selective pulse.

The consequence of having increased chemical shift displacement errors is more severe in a non-homogeneous sample like brain as opposed to a homogeneous sample like phantoms. Even in the case of NAA and Creatine where the majority of signal contribution comes from the singlet peak, a big difference in [NAA/tCr] ratio was observed in this study. Incoherent averaging is not the only contributor of this difference; the shifted volume could have a different composition of grey matter, white matter and cerebrospinal fluid (CSF) and different metabolite concentrations.

Calculation of bandwidth requirements at 7 Tesla shows that a refocusing pulse bandwidth of 5126 Hz at 7 Tesla would result in chemical shift displacements that equal

those from 3 Tesla for the pulses and B1 used in this study. The measured [met/tCr] ratio would likely be smaller at 7 Tesla compared to 3 Tesla despite having a comparable pulse bandwidth due to the differences in T1 and T2 relaxation rates at the two field strengths and increased B1 and B0 inhomogeneities at 7 Tesla. However, the decreased macromolecule contamination, increased SNR and increased spectral resolution offered at 7 Tesla could potentially help in quantification of metabolites with higher precision, provided we can implement pulses with higher bandwidth that are insensitive to B1 homogeneities.

4.4 Conclusions

Our results show significant discrepancies in the metabolite-to-creatine ratios measured at 3 Tesla and 7 Tesla with the pulses and bandwidths used in this study. Increasing the bandwidth of the pulses reduces the chemical shift displacement errors and differences between the measurements made at 3 Tesla and 7 Tesla. Our study shows strong evidence of the requirement of having the bandwidth of the pulses comparable to that used on 3 Tesla for making better measurements at 7 Tesla. For the parameters used in this study, having slice-selective refocusing pulse bandwidths equal to or greater than 5126 Hz at 7 Tesla would potentially yield measurements with higher precision and help realize the benefit of going to 7 Tesla.

CHAPTER V

TIME-RESOLVED MRS

5.1 Introduction

The human brain constitutes of 2% of the body's mass but consumes almost 20% of the body's energy metabolism at rest (*43*). Functional Magnetic Resonance Imaging (fMRI) studies have helped identify those areas of the brain that increase neural activity during specific stimulations through the detection of corresponding hemodynamic changes (*44*). The study of hemodynamic changes, while of great importance, provides only an indirect measure of neuronal activity. Functional Magnetic Resonance Spectroscopy (fMRS) measurements have the potential of providing insights into the coupling between neuronal activity and metabolism and to the underlying biochemical changes that follow from changes in neural activation. There have been a number of previous studies performed to study the changes in metabolite profile during regional activation (*14, 45-51*) but these have had limited sensitivity and have used prolonged periods of activation, and thus cannot reveal any transient changes that might occur immediately after a stimulating event.

Measurement of concentrations for some metabolites is difficult due to their low concentration, for example, lactate and glucose. The overlap in signals from different metabolites also poses difficulty for accurate measurement of concentrations. Hence, optimizing the measurement parameters and sensitivity is crucial for measuring metabolite concentrations as well as the changes in metabolite concentrations, which are likely to be even smaller.

Due to the inherently low sensitivity of MRS measurements, averaging a number of transients is essential in order to achieve spectra with high enough signal-to-noise ratios (SNR) to accurately quantify metabolite concentrations. Thus a series of spectra cannot in general be acquired with high temporal resolution. Most previous studies have used block paradigms to study neuroenergetics. Averaging spectra acquired over an extended period is appropriate for measuring metabolite changes that are sustained for longer durations but will miss any transient changes that happen within the activation block. The highest temporal resolution reported for a functional magnetic resonance spectroscopy study to-date is 20 s (*48*). This leaves unanswered questions as to what may be happening in terms of neuroenergetics immediately after the onset of stimulus. For example, although some metabolites may change on average slowly as a result of continuing stimulations, over shorter times there may be larger increases and subsequent decays or wash-out that are undetected. Thus there is a need for a method that increases temporal resolution of functional MRS studies. Similar considerations have arisen in the field of functional MRI wherein the use of event-related designs allow temporal resolution of transient events that can be repeated.

The aim of this study was to implement a unique event-related binning method to measure transient changes in metabolite concentrations during regional activation with increased temporal resolution. The binning method used in the study increases the effective temporal resolution significantly such that the temporal resolution is limited by the repetition time of the pulse sequence, and the SNR by the number of events that can be repeated in practice.

5.2 Method

Twelve volunteers were scanned in accordance with the protocol approved by the Vanderbilt University Institutional Review Board on a 3 Tesla Philips Achieva MR Scanner. A birdcage transmit/receive coil with a 30.0 cm diameter was used with a maximum B1 of 23.5 μT.

5.2.1 Imaging

Anatomical images were acquired using T1-weighted turbo field echo (TFE) sequence with 1x1x2 mm^3 resolution, TE/TR = 3.19/6.54 ms, field-of-view (FOV) size = 240x240x170 mm^3, number of slices = 85 with 64x63 pixels, water-fat shift = 2.02 pixels for a scan time of 5 minutes. All anatomical images were acquired in saggital planes and reformatted to generate axial and coronal planes for better voxel placement.

Functional MRI data sets were acquired using a T2*-weighted gradient-echo echo planar imaging sequence (GE-EPI) with the following parameters: FOV = 220 mm, TE/TR = 35/2000 ms, number of slices = 30, slice thickness = 3 mm, slice gap = 0.5 mm, 30 slices. All functional images were axially oriented. A full field-of-view black and white radial checkerboard flashing at 8 Hz frequency was used as stimulus for all the functional scans. The fMRI runs consisted of six blocks of 40 seconds each, where each block had 20 seconds of stimulus followed by 20 seconds of rest culminating in a total of 240 seconds of scan time and 120 dynamics. IViewBold tool in the Philips MR scanner was used to generate activation maps in real-time during functional MRI sequences and the activation maps generated using IViewBold was used as a guide to place the voxels for acquiring spectral data.

5.2.2 Spectroscopy

Water unsuppressed spectra

70 transients of water unsuppressed spectra were acquired in a series that consisted of 3 cycles of 20 s rest followed by 20 s of stimulus at TE/TR = 60/3000 ms from the activation region to confirm the accuracy of the voxel placement using a PRESS sequence. Water peak height and corresponding water linewidth were calculated using custom-built programs written in MATLAB to ensure the voxel was placed in an activated region that demonstrated a BOLD response in the water spectra. The water scan was repeated at the end of the study as a quality control measure. Any data set that lacked a BOLD response at the end of the scan reflected subject motion during the scan and the data were excluded from further analyses.

Metabolite spectra

Subjects were scanned using two paradigms: the first constituted a block paradigm and the second consisted of an event-related paradigm.

Block paradigm

Metabolite spectra were acquired from the activated region using a MEGA-PRESS sequence for lactate editing (*3*). An editing pulse with 64 Hz bandwidth was applied and the editing frequency was toggled between +/- 60 Hz to produce a refocused lactate peak at 1.3 ppm on odd scans. Editing frequency was set to -60 Hz during odd scans and to +60 hz during even scans. Water suppressed functional MR spectra were acquired with an initial 4 minute resting state block followed by two cycles of 8 minutes of activation

blocks and 8 minutes resting state blocks. Each transient was saved separately and were corrected for frequency and phase variations with the Creatine peak as the reference peak using custom-built programs written in MATLAB (*4*). The data were binned into 2 sets: 8 minute blocks and one-minute blocks, after which odd and even spectra were generated for each of the blocks.

Event-related paradigm

The paradigm consisted of 32 cycles of 32 seconds of activation followed by 32 seconds of rest. A MEGA-PRESS sequence with editing pulse at 4.1 ppm resonance frequency to refocus the lactate peak at 1.3 ppm and TE/TR = 73/2000 ms was used to acquire water suppressed spectra from the activated region. Each transient was saved separately and was frequency and phase corrected using custom-built programs written in MATLAB. The data were binned based on the time of acquisition after the onset of stimulation in order to achieve an effective temporal resolution that equals the repetition time of the scans. A schematic diagram of the binning strategy is shown in Figure 5.1. The binning method averages data points from all the functional cycles collected at the j^{th} time point, and the process is repeated for each time point. The resulting spectra have a temporal resolution that equals the repetition time of the pulse sequence.

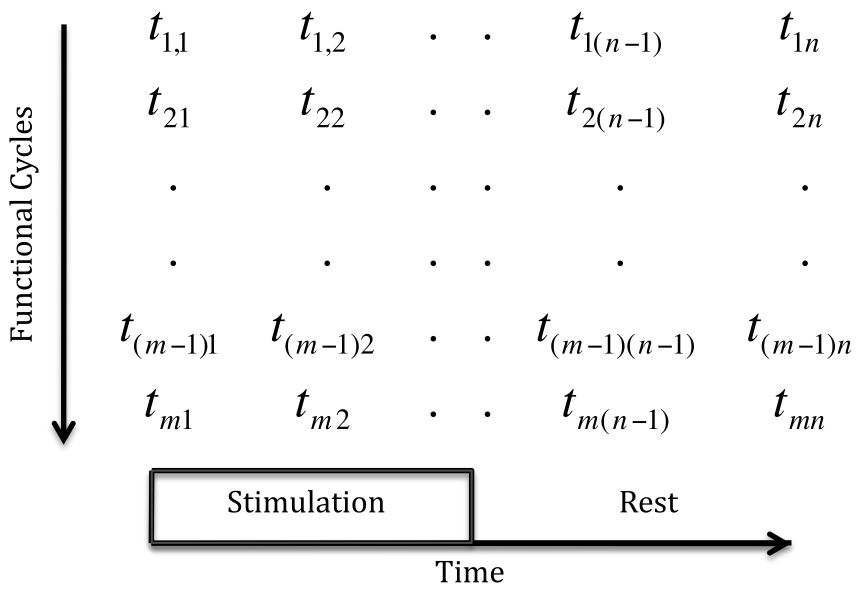

Figure 5.1. Schematic diagram of the binning method for event-related paradigm, where the scan consisted of m functional cycles and each functional cycle consisted of n time points. t_{ij} represents j^{th} data collected after the onset of stimulation during i^{th} functional cycle.

5.2.3 Data analysis

A simulated basis set for use with LCModel for analyzing the data was generated for echo-time = 73 ms for the MEGA-PRESS sequence with an editing pulse of 64 Hz bandwidth applied at 1.3 ppm, using programs written in C++ using GAMMA tools (*17, 19*). The simulation incorporated ideal slice selective pulses and real editing pulses. FIDs from 8000 gradient points were summed to include the effect of crusher gradients on the spin resonances in the presence of frequency selective pulses. All the data sets were zero-filled to 8192 points and an exponential filter of 2 Hz was applied to the time–domain signals to reduce the noise. The resulting spectra were analyzed using LCModel for both the studies; block paradigm and event-related paradigm. NAA peaks from the event-related paradigm with 2 s temporal resolution were analyzed using a custom-built

program written in MATLAB and the results grouped as activation and rest to calculate average and standard deviation values for peak height, linewidth, and area.

Statistical Methods

The differences in [met]/[tCr] ratios were estimated using a mixed-effect model for data binned in 1 minute blocks for the block paradigm and the data for the event-related paradigm using a restricted maximum likelihood (REML) method.

5.2.4 Detection threshold determination

Theoretical CRLBs for a set of 17 metabolites were calculated using the basis set generated for analyzing the data for the study. CRLB calculations were performed using the average metabolite concentrations report in the literature and linewidths and SNR typically observed in this study. The CRLBs were used to determine the sensitivity of the study to measure changes in metabolite concentrations during regional activation.

5.3 Results and discussion

5.3.2 Block paradigm

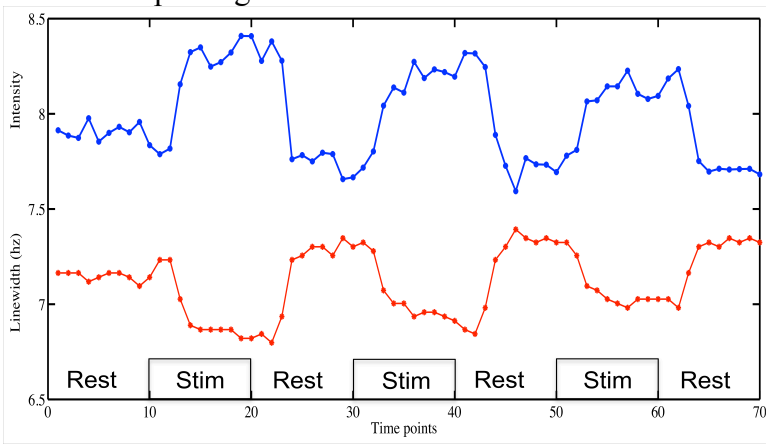

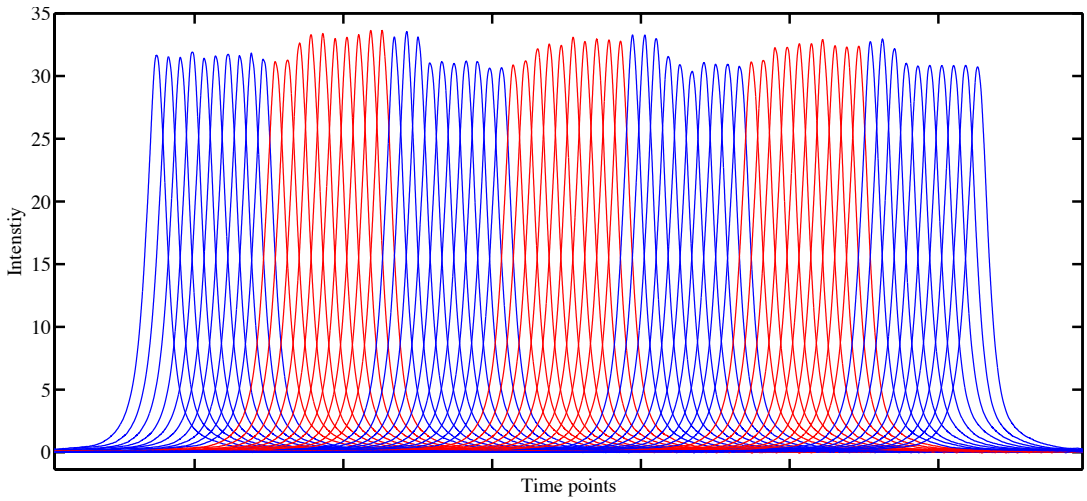

Figure 5.2. (Top) Water peak height (blue) and water line widths (red) during activation and rest blocks. (Bottom)Water spectra acquired during 3 cycles of 30 seconds of activation (red) followed by 30 seconds of rest (blue) showing BOLD response.

Figure 5.2 shows the increases in peak heights and corresponding decreases in linewidths of water spectra during activation that return to baseline during rest. This is a measurement of the BOLD response from the water signal using MRS and confirms the accuracy of the voxel placement in the region activated during visual stimulation. The temporal resolution of water-unsuppressed spectra was 3 s and we observed a lag in the

beginning of the BOLD response between 6 and 9 s , and between 9 and 12s for the water peak height to decrease and linewidth to increase after the end of stimulus. Average change in the water peak height and water linewidth during activation were: +2.92% and -2.48% respectively.

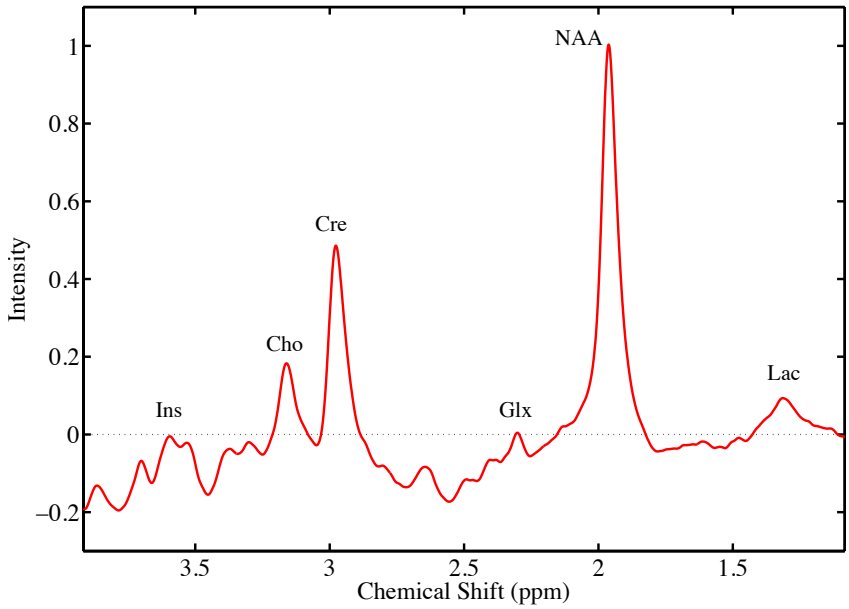

Figure 5.3. In vivo spectra acquired from the visual cortex using MEGA-PRESS sequence with editing frequency at -60 Hz and editing pulse bandwidth of 64 Hz. 120 transients were averaged to generate each spectra at TE/TR = 73/2000 ms.

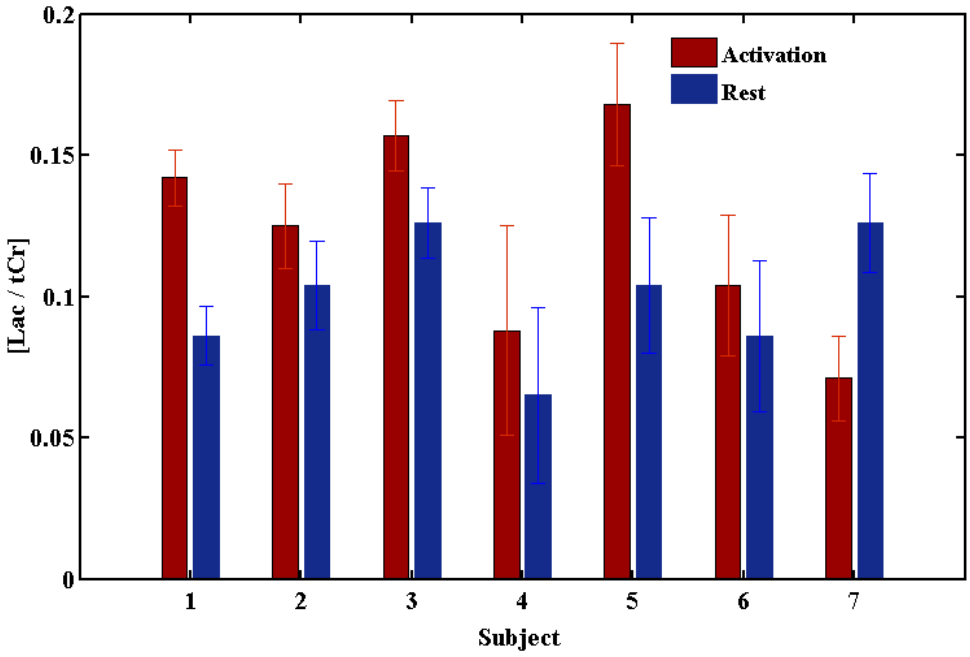

Figure 5.4. LCModel results for Lactate to Creatine ratio for 7 subjects showing increase in lactate concentration during stimulus (red) compared to rest (blue) for 6 of the 7 volunteers.

Representative spectra are shown in Figure 5.3 which shows the typical signal-to-noise ratio achieved during the scans in this study. Results from LCModel showing an increase in lactate concentration during activation in 6 of the 7 volunteers scanned for this paradigm are shown in Figure 5.4. An average change in lactate concentration for 7 volunteers was 26.3 ± 21.6% consistent with the increases reported in the recent studies (*48, 52*). While analysis of spectra from averaging two 8 minute blocks shows increases in lactate for most of the volunteers during the activation period, statistical analysis of 1 minute blocks did not show significant change in any of the metabolites during block stimulus.

5.3.2 Event-related paradigm

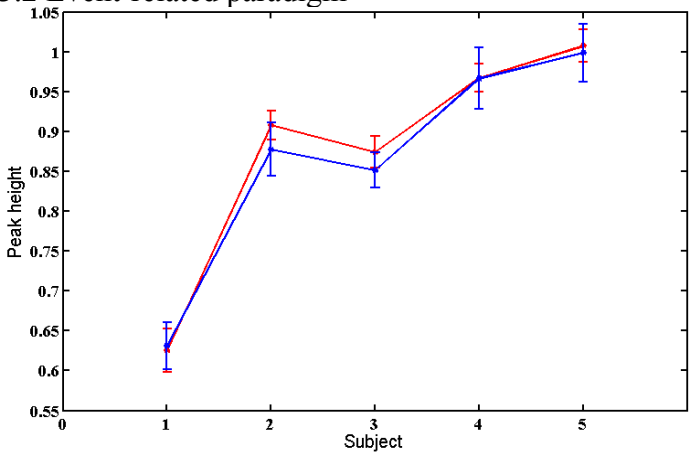

a)

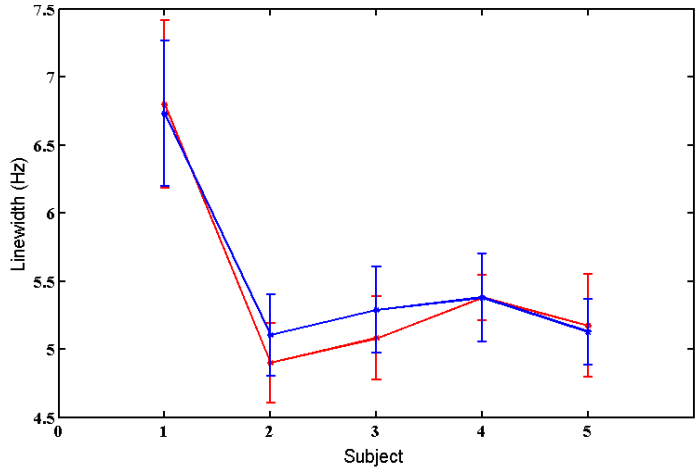

b)

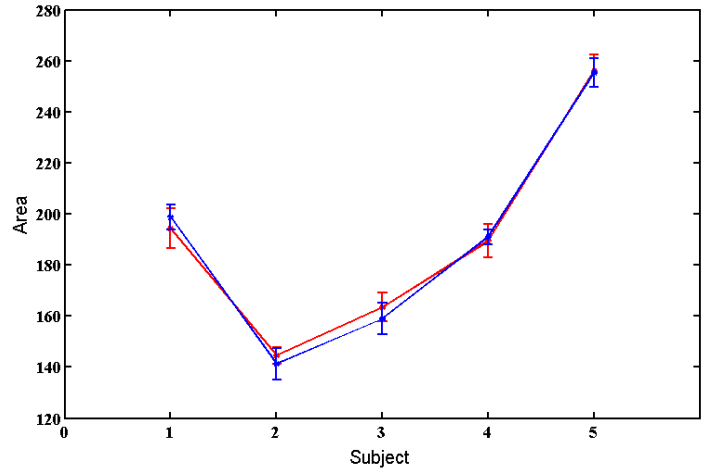

c)

Figure 5.5. Results from peak analysis showing a) peak height, b) linewidth, and c) area under the NAA peak during activation (red) and rest (blue) for 5 subjects.

Figure 5.5 a, b and c show the increases in peak height, decreases in linewidth and non-significant differences in areas of the NAA peak during activation compared to rest periods in 5 subjects. These NAA results are consistent with the results reported by Zhu et al (*51*). We observed between an 8-10 s second delay in the observed increase in the NAA peak height after the onset of stimulation consistent with the delay in hemodynamic response as well as an 8-10 s delay in the decrease in the NAA peak back to baseline after the end of stimulation. The time delays for observance of changes due to BOLD response from analysis of water spectra and NAA in this study are comparable.

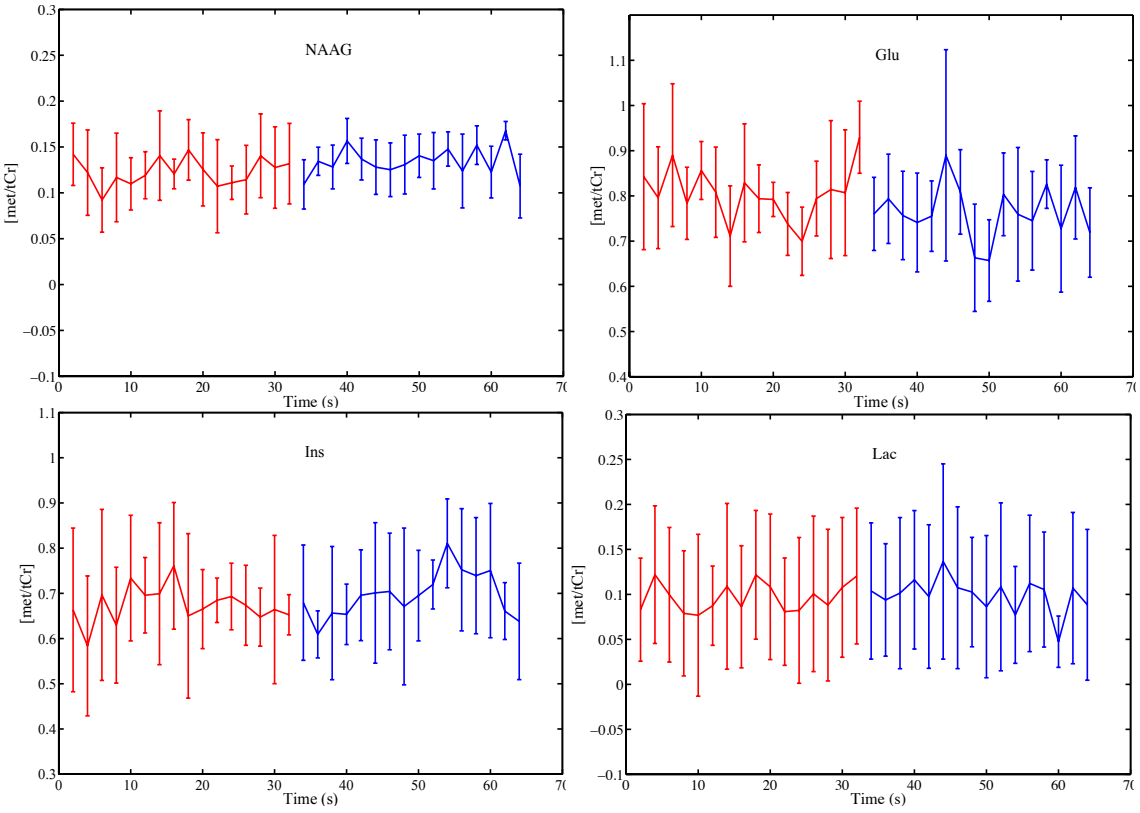

Figure 5.6. Metabolite time courses with 2 s resolution during activation (red) and rest (blue) periods averaged across 5 subjects.

Figure 5.6 show metabolite concentrations as a function of time during periods of activation and rest averaged across 5 subjects. Statistical analysis of LCModel results of spectra with 2 s temporal resolution shows 5.37% ± 2.32% ($p < 0.05$) increase in Glu and -8.21% ± 3.74% ($p < 0.05$) decrease in NAAG during activation. Our analysis did not correct for any variation in linewidth during the activation period and we did not observe a significant change in NAA to Creatine ratios between activation and rest periods.

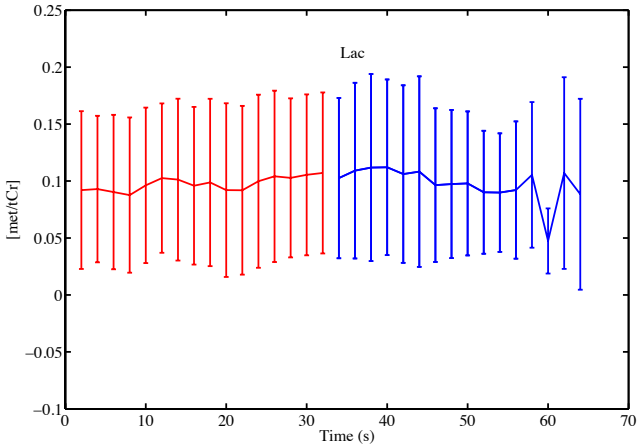

Figure 5.7. Running average of 5 time points of [lac/tCr] as a function of time from 5 subjects. Red plot represents [lac/tCr] area during 32 s of activation and blue during 32 s of rest. The last 4 points in the plot only consist of data from 1 time point.

Running averages of 5 time points of [lac/tCr] from LCModel averaged over 5 subjects show a gradual increase in lactate concentration during activation and can be observed in Figure 5.7. An increase in [lac/tCr] was observed in the running average plot after 8 s of stimulation. The increase level of [lac/tCr] persisted until about 14 s after the end of stimulation followed by a decrease back to baseline levels. While an increase in lactate level was observed in the plot with running average of 5 time points, the results were not statistically significant when analyzing individual time points.

The detection limitation of the current experiment based on the theoretical CRLB for lactate is 6.32%, glutamate is 2.73% and for NAAG is 2.54%. Given the sensitivity of detection in change of lactate concentration of 6.32%, our observation of 26.30% increase in lactate during a prolonged stimulation of 8 minute, confirm the increased lactate levels during prolonged activation. At shorter time scales of 16 s and 32 s, we did not observe increases in lactate levels with statistical significance despite our observation of increases in lactate levels from the running average plot suggests the need for a larger sample size to reach statistical significance.

Our results show that the binning method employed in this study improved the temporal resolution of the functional MRS study. However, despite the use of this novel binning method and the short duration of the functional trial, data from individual subjects did not contain enough SNR to effectively study changes in metabolite profiles during activation. Datasets from 5 subjects were used to perform the analysis. Given the restriction of the scan time on a volunteer, the full benefit of using this binning method for fMRS studies will be realized by increasing the number of data sets thereby increasing the number of samples per time point.

5.4 Conclusions

Our results show that the binning method employed in this study is an effective way to increase temporal resolution in fMRS measurements. BOLD changes in water spectra and NAA peak are observed during activation and provide a robust quality control criteria for ensuring acquisition of data from the activated region. We observed increases in Lactate concentrations during prolonged stimulation and as well as during 32 s of stimulation

although not with strong statistical significance. We also observed increases in glutamate during 32 s of stimulation and simultaneous decreases in NAAG with statistical significance. To our knowledge, these are the first reported measurements made with 2 s temporal resolutions, and increasing the number of samples per time point can help make robust measurements on changes in metabolite profile with statistical significance even at 2 s temporal resolution.

CHAPTER VI

CONCLUSION

MRS is a powerful tool for non-invasive measurements of metabolite concentrations in the brain. However, the low SNR of spectra coupled with spectral overlap between different metabolites necessitates careful evaluation of the effects of experimental parameters while for some metabolites, specialized pulse sequences and data analysis techniques must be developed. Material presented in this dissertation is aimed to improve measurements and quantification of metabolites, neurotransmitters in particular, through different approaches.

6.1 Numerical evaluation of optimal detection parameters

One of the approaches used for improving metabolite detection is moving to higher field strengths. Increased static magnetic fields result in increased spectral dispersion and also increased SNR because the resonance frequency is directly proportional to the static magnetic field strength while SNR increases in a more complex manner than depends on several factors. However, the move to higher field strength needs to be accompanied by the use of optimal measurement parameters to realize the full benefit of the move and at higher fields some technical challenges become more severe. At higher field strength, B0 and B1 inhomogenieties become increasingly worse, transverse relaxation rates faster and the requirement for pulse bandwidth higher. Calculation of theoretical CRLBs for a range of parameters of interest is an efficient method of assessing optimal measurement parameter values

Chapter 3 of this thesis evaluated the optimal echo-times for detection of 18 metabolites using PRESS sequence at 7 Tesla using simulated spectra for echo-times in the range of 30-180 ms and calculating the theoretical CRLBs at each echo-time. Our results show that while the optimal echo-time for detecting most metabolites is 30 ms, the optimal echo-time for glutamate is 109 ms, glutamine is 110 ms, and 2-hg is 96 ms and the worst echo-time for making metabolite measurements using PRESS sequence at 7 Tesla is clustered around 50 ms.

Our study evaluated the optimal detection echo-time for making metabolite measurements using PRESS sequence at 7 Tesla; however, the CRLB calculation method used for this study is very versatile. CRLB calculations could be performed using the methods described in this chapter for any pulse sequence and any set of parameters and the results can be used to identify the optimal parameters like pulse sequence, echo-times etc with great efficiency. These CRLB calculations can also be used to test the feasibility of a new pulse sequence to detect our metabolite of interest and aid in the implementation of methods and parameters that give the highest precision for the metabolite.

6.2 GABA measurements at 3 Tesla and 7 Tesla

As we move to higher fields, apparent differences in quantification results between different field strengths arise and need to be understood. Assessment of the differences and the parameters affecting the measurements will help address those issues.

Chapter 4 of this thesis reported results from the comparison between GABA measurements made at 3 Tesla and 7 Tesla and the requirement for making measurements with higher precision at 7 Tesla. Comparison of metabolite measurements

made at 3 Tesla and 7 Tesla show large discrepancies in the concentrations. Increasing the bandwidth of the pulses by small amounts mitigated these discrepancies slightly, which showed that chemical shift displacement errors due to inadequate bandwidth of the slice-selective pulses was one of the main explanations for this discrepancy. The results show that the full benefit of transitioning to higher field strength of 7 Tesla from 3 Tesla can only be realized with the use of pulses that are of comparable bandwidth to those used at 3 Tesla.

For the pulses used for this study, the bandwidth requirement on slice-selective refocusing pulses at 7 Tesla to achieve chemical shift displacements equal to that observed at 3 Tesla was 5126 Hz. Given the limitation on maximum B1 that can be used at 7 Tesla, specialized pulses with bandwidths higher than 5126 Hz need to be developed and implemented to potentially make better metabolite measurements at 7 Tesla compared to 3 Tesla.

6.3 Changes in metabolite profile during neuronal activation

The detection of changes in metabolite concentrations during neuronal activation can help understand the coupling between neuronal activity and oxygen metabolism. Study of these concentration changes demand a method that yields a high enough temporal resolution to be able detect transient changes with high temporal resolution. Due to the low sensitivity of MRS measurements, obtaining data sets with high temporal resolution has been elusive with the highest temporal resolution reported in the literature at 20 s.

A method of significantly increasing the effective temporal resolution of fMRS measurements was presented in Chapter 5 of this thesis. By using an event-related

binning method where the data are binned based on the time point after the onset of stimulation, a temporal resolution that equals the repetition time of the pulse sequence was achieved. For the experiment presented in Chapter 5, the temporal resolution was 2 s. However, such high temporal resolution in practice was not possible because of low SNR. Our results showed increase in glutamate and decrease in NAAG during 32 s of activation period compared to the 32 s of resting period with statistical significance. When grouping the timepoints into 16 s blocks, we observed a gradual decrease in myo-Inositol during 32 s of activation that gradually increased possibly back to baseline levels, after the end of stimulation period with statistical significance. We did not observe any change in lactate levels during the 32 s of activation followed by 32 s of rest. The changes we observed with statistical significance were higher than the limitation on the precision of our measurement dictated by the CRLB calculations, which indicates these observed changes were real.

These results were derived from data acquired from 5 volunteers and we were not able to observe changes in metabolite concentrations that were statistically significant possibly due to the small number of volunteers. Acquisition of data from a larger number of volunteers would help increase the number of samples at each timepoint and evaluate the change in metabolites with 2 s temporal resolution and reach a statistical significance on the analysis of transient change in metabolite profile during neuronal activation.

6.4 Future directions

One of the limitations of MRS studies is the low SNR that results in long acquisition times. With the emergence of 7 Tesla, there is potential for achieving higher SNR since

it scales linearly with static magnetic field strength. The cumulative work done as part of this thesis will aid in the improvement of the data acquired at 7 Tesla. Application of the optimal detection parameters along with high bandwidth pulses at 7 Tesla will help acquire data with high SNR and increased spectral resolution. Tailoring the pulse sequences and echo-times based on the metabolite of interest, employing pulses with high bandwidth will help acquire spectra with higher precision and accuracy at 7 Tesla. This strategy could also be a solution to study metabolite changes during neuronal activation more reliably by taking advantage of increased SNR at 7 Tesla.

Transient changes in metabolite profile during neuronal activation is of interest and based on the results presented on this thesis the following steps should be taken to make better measurements at 7 Tesla. Optimal pulse sequence and echo-times at 7 Tesla for measuring lac, glc, glu and ins should be investigated using CRLB calculations and the pulse sequences implemented at 7 Tesla if not already available and slice-selective pulses with high bandwidth should be developed to reduce the chemical shift displacement errors.

APPENDIX

APPENDIX A. EXAMPLES

Appendix A.1

Spin systems need to be specified in order to perform density matrix simulations on that spin system. An example of spin system specified for use with GAMMA libraries is shown below.

```
SysName    (2) : 2spin      - Name of the Spin System
NSpins     (0) : 2                  - Number of Spins in the System
Iso(0)     (2) : 1H              - Spin Isotope Type
Iso(1)     (2) : 1H              - Spin Isotope Type
J(0,1)     (1) : 7.0        - Scalar Coupling (Hz)
PPM(0)     (1) : 2.00       - Chemical Shift (PPM)
PPM(1)     (1) : 3.00       - Chemical Shift (PPM)
Omega      (1) : 128        - 1H Static Field Strength
```

Appendix A.2

An example of a program that performs density matrix simulation using ideal pulses written in C++ using GAMMA libraries is shown below.

```
#include <gamma.h>
//#include "engine.h"
//#include <string>
using namespace std;
main(int argc, char*argv[])
{
spin_system sys;                        // Declare a spin system
sys.read(sys_fname+sys_ext);            // Reading the spin system
```

```
double sw = 10000.;              // spectral width in hz
double ppm = sw / sys.Omega();   // setting spectral width
NyqF = sw * 2.0;                 // Nyquist frequency
// acquisition blocks
block_1D data_Fx(t2pts);         // x-channel acquisition
block_1D data_Fy(t2pts);         // y-channel acquisition
gen_op sigma0;    // initial and  working density operator
gen_op H = Ho(sys);              // Set up Hamiltonian   gen_op Dx = Fx(sys);
          // Detect Fx
gen_op Dy = Fy(sys);          // Detect Fy
double TE = 0.073;                              // Define TE          double tau1 = 0.008;
         // Define tau1
double tau2 = TE/2.0-TE1;             // Define tau2          sigma0 = sigma_eq(sys);
             // Set the density matrix to equilibrium
sigmap = Iypuls(sys,sigma0,90.0);// Apply 90 degree pulse
sigmap = evolve(sigmap,H,tau1);  // Evolve density matrix
sigmap = Ixpuls(sys,sigmap,180.0);// Apply 180 degree pulse
sigmap = evolve(sigmap,H,tau1);  // Evolve density matrix
sigmap = evolve(sigmap,H,tau2);
sigmap = Ixpuls(sys,sigmap,nsrefo);
sigmap = evolve(sigmap,H,tau2);
row_vector t2BLK_Fx = FID(sigmap,Dx,H,1/(sw),t2pts);
                                                // FID acquisition
data_Fx.put_block(step, 0, t2BLK_Fx);
data_Fy.put_block(step, 0, t2BLK_Fy);
// Saving Output to Matlab
MATLAB( out_fname+"_Fx.mat",  "data", data_Fx, 0 );
MATLAB( out_fname+"_Fy.mat",  "data", data_Fy, 0 );
```

Appendix A.3

An example of a program that performs density matrix simulation using real pulses written in C++ using GAMMA libraries is shown below.

```
#include <gamma.h>
//#include "engine.h"
//#include <string>
using namespace std;
main(int argc, char*argv[])
{
spin_system sys;                        // Declare a spin system
sys.read(sys_fname+sys_ext);            // Reading the spin system
double sw = 10000.;              // spectral width in hz
double ppm = sw / sys.Omega();   // setting spectral width
NyqF = sw * 2.0;                 // Nyquist frequency
// acquisition blocks
block_1D data_Fx(t2pts);         // x-channel acquisition
block_1D data_Fy(t2pts);         // y-channel acquisition
gen_op sigma0;    // initial and  working density operator
gen_op H = Ho(sys);              // Set up Hamiltonian   gen_op Dx = Fx(sys);
          // Detect Fx
gen_op Dy = Fy(sys);          // Detect Fy
double TE = 0.073;                          // Define TE          double tau1 = 0.008;
         // Define tau1
double tau2 = TE/2.0-TE1;             // Define tau2
double ex_dur = 0.0040;               // excitation pulse duration
double refo_dur = 0.0060;             // refocusing pulse duration
double Wrf = -789.0                   // Set center frequency
sigma0 = sigma_eq(sys);
             // Set the density matrix to equilibrium
```

```
matrix ex_wave = MATLAB("spredrex.mat", "a");
                                        //Define excitation pulse shape
matrix refo_wave = MATLAB("gtst1203.mat", "a");
                                        //Define refocusing pulse shape
row_vector ex_amp(transpose(ex_wave));
row_vector refo_amp(transpose(refo_wave));
ex_U = Shxypuls_U(sys,ex_amp,H,sys.symbol(0),Wrf,ex_dur,90.0,90.0);
                                        // Set excitation pulse attributes
sigmap  = evolve(sigma0,ex_U);              // Apply excitation pulse
sigmap  = evolve(sigmap,H,tau1 – ex_dur/2.0 - refo_dur/2.0);
                                                    // Evolve density matrix
refo1_U = Shxypuls_U(sys,refo_amp,H,sys.symbol(0), Wrf, refo_dur, 180.0, 180.0);
        // Set refocusing pulse attributes
sigmap  = evolve(sigmap,refo1_U);   // Apply refocusing pulse
sigmap  = evolve(sigmap,H,tau1 - (refo_dur/2.0));
                                                    // Evolve density matrix
sigmap  = evolve(sigmap,H,tau2 - (refo_dur/2.0));
                                                    // Evolve density matrix
refo2_U = Shxypuls_U(sys,refo_amp,H,sys.symbol(0),Wrf,refo_dur, 180.0,180.0);
        // Set refocusing pulse attributes
sigmap = evolve(sigmap,refo2_U);            // Apply refocusing pulse
sigmap = evolve(sigmap,H,tau2 - (refo_dur/2.0));
                                                    // Evolve density matrix
row_vector t2BLK_Fx = FID(sigmap,Dx,H,1/(sw),t2pts);
                                                    // FID acquisition
data_Fx.put_block(step, 0, t2BLK_Fx);
data_Fy.put_block(step, 0, t2BLK_Fy);
// Saving Output to Matlab
MATLAB( out_fname+"_Fx.mat",  "data", data_Fx, 0 );
MATLAB( out_fname+"_Fy.mat",  "data", data_Fy, 0 );
```

Appendix A.4

An example of a *makebasis.IN* file is shown below.

```
$SEQPAR
 echot=73.
 seq='PRESS'
 fwhmba=0.01
 $END

 $NMALL
 HZPPPM=298.000000
 DELTAT=0.0001000
 NUNFIL=16384
 FILBAS='.lcmodel/simulation/output/JDIFF_GABA_7T.basis'
 FILPS='.lcmodel/simulation/output/JDIFF_GABA_7T.ps'
 AUTOSC=.false.
 AUTOPH=.false.
 IDBASI='MEGA-PRESS GABA simulated basis set'
 $END

 $NMEACH
 FILRAW='.lcmodel/simulation/raw/jdiff_7T/asp.RAW'
 METABO= 'Asp'
 DEGZER = 0.
 DEGPPM = 0.
 CONC=0.1
 CONCSC=100.
 PPMAPP=0., -.04
 $END

 $NMEACH
 FILRAW='.lcmodel/simulation/raw/jdiff_7T/gaba.RAW'
 METABO= 'GABA'
 DEGZER = 0.
 DEGPPM = 0.
 CONC=0.1
 CONCSC=100.
 PPMAPP=0., -.04
 $END

 $NMEACH
 FILRAW='.lcmodel/simulation/raw/jdiff_7T/gln.RAW'
 METABO= 'Gln'
 DEGZER = 0.
 DEGPPM = 0.
```

```
CONC=0.1
CONCSC=100.
PPMAPP=0., -.04
$END

$NMEACH
FILRAW='.lcmodel/simulation/raw/jdiff_7T/glu.RAW'
METABO= 'Glu'
DEGZER = 0.
DEGPPM = 0.
CONC=0.1
CONCSC=100.
PPMAPP=0., -.04
$END

$NMEACH
FILRAW='.lcmodel/simulation/raw/jdiff_7T/gsh.RAW'
METABO= 'Gsh'
DEGZER = 0.
DEGPPM = 0.
CONC=0.1
CONCSC=100.
PPMAPP=0., -.04
$END

$NMEACH
FILRAW='.lcmodel/simulation/raw/jdiff_7T/naa.RAW'
METABO= 'NAA'
DEGZER = 0.
DEGPPM = 0.
CONC=0.1
CONCSC=100.
PPMAPP=0., -.04
$END

$NMEACH
FILRAW='.lcmodel/simulation/raw/jdiff_7T/naag.RAW'
METABO= 'NAAG'
DEGZER = 0.
DEGPPM = 0.
CONC=0.1
CONCSC=100.
PPMAPP=0., -.04
$END
```

APPENDIX B. SUPPLEMENTARY MATERIAL

Appendix B.1

Concentration and corresponding CRLB measurements for a set of 17 metabolites in Chapter 3.

TE (ms)	Ala	Asp	Cre	GABA	Glc	Gln	Glu	GPC	Gsh	Lac	Ins	NAA	NAAG	PCh	PCr	Scyllo	Tau
Conc. (mM)	1.2	1.2	8.0	1.5	1.0	4.5	10.0	1.0	2.0	1.0	6.5	15.0	2.0	2.0	4.0	0.5	1.2
T2 = 109 ms																	
30	6.7	18.5	1.2	11.1	14.3	7.6	2.5	6.1	3.5	8.3	1.2	0.3	2.2	3.1	2.4	4.8	8.9
109	8.4	28.6	2.6	9.1	33.8	4.1	1.7	12.1	4.9	10.3	3.4	0.7	4.6	6.1	5.1	9.8	14.8
T2 = 158 ms																	
30	6.2	17.0	1.1	10.2	13.1	7.0	2.3	5.6	3.2	7.6	1.1	0.3	2.0	2.8	2.2	4.4	8.2
109	6.1	21.0	1.9	6.6	24.8	3.0	1.2	8.9	3.6	7.5	2.5	0.5	3.3	4.5	3.7	7.2	10.9

Appendix B.2

Dependence of metabolite CRLBs on echo-time for T_2 = 109 ms for a set of 17 metabolites calculated for echo-times in the range of 30-150 ms with concentrations shown in Appendix B.1 is shown below.

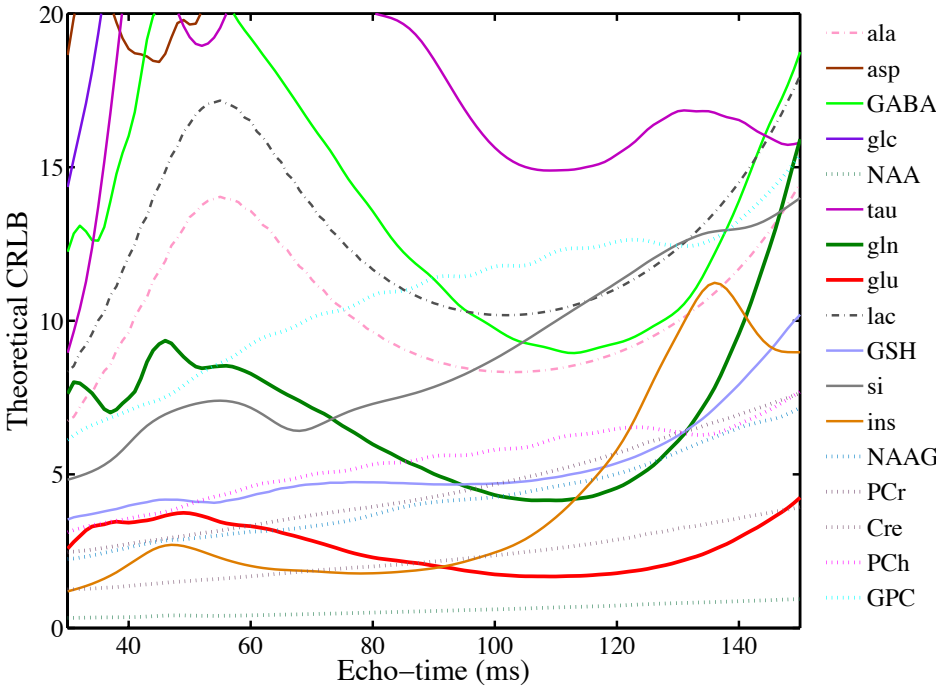
Theoretical CRLB
Echo–time (ms)
0
5
10
15
20
40
60
80
100
120
140
ala
asp
GABA
glc
NAA
tau
gln
glu
lac
GSH
si
ins
NAAG
PCr
Cre
PCh
GPC

REFERENCES

1. Levitt, M. H. (2003) *Spin Dynamics: Basics of Magnetic Resonance*, 3rd ed.

2. de Graaf, R. A. (2007) *in Vivo NMR Spectroscopy: Principles and Techniques*, John Wiley & Sons Ltd.

3. Mescher, M., Merkle, H., Kirsch, J., Garwood, M., and Gruetter, R. (1998) Simultaneous in vivo spectral editing and water suppression, *NMR in Biomedicine 11*, 266-272.

4. Waddell, K. W., Avison, M. J., Joers, J. M., and Gore, J. C. (2007) A practical guide to robust detection of GABA in human brain by J-difference spectroscopy at 3 T using a standard volume coil, *Magn. Reson. Imaging 25*, 1032-1038.

5. Terpstra, M., Henry, P.-G., and Gruetter, R. (2003) Measurement of reduced glutathione (GSH) in human brain using LCModel analysis of difference-edited spectra, *Magnetic Resonance in Medicine 50*, 19-23.

6. Behar, K. L., Rothman, D. L., Spencer, D. D., and Petroff, O. A. C. (1994) Analysis of macromolecule resonances in 1H NMR spectra of human brain, *Magnetic Resonance in Medicine 32*, 294-302.

7. Mader, I., Seeger, U., Karitzky, J., Erb, M., Schick, F., and Klose, U. (2002) Proton magnetic resonance spectroscopy with metabolite nulling reveals regional differences of macromolecules in normal human brain, *Journal of Magnetic Resonance Imaging 16*, 538-546.

8. Vaughan, J. T., Garwood, M., Collins, C. M., Liu, W., DelaBarre, L., Adriany, G., Andersen, P., Merkle, H., Goebel, R., Smith, M. B., and Ugurbil, K. (2001) 7T vs. 4T: RF power, homogeneity, and signal-to-noise comparison in head images, *Magn. Reson. Med. 46*, 24-30.

9. Ellis C.M., Lemmens, G., Williams, S. C., Simmons, A., Dawson, J., Leigh, P. N., and Chaudhuri, K. R. Changes in putamen N-acetylaspartate and choline ratios in untreated and levodopa-treated Parkinson's disease: a proton magnetic resonance spectroscopy study.

10. Giroud M., Walker, P., Bernard, D., Lemesle, M., Martin, D., Baudouin, N., Brunotte, F., and Dumas, R. Reduced brain N-acetyl-aspartate in frontal lobes suggests neuronal loss in patients with amyotrophic lateral sclerosis.

11. Waddell, K. W., Zanjanipour, P., Pradhan, S., Xu, L., Welch, E. B., Joers, J. M., Martin, P. R., Avison, M. J., and Gore, J. C. (2011) Anterior cingulate and

cerebellar GABA and Glu correlations measured by 1H J-difference spectroscopy, *Magn. Reson. Imaging 29*, 19-24.

12. Auer, D. P., Putz, B., Kraft, E., Lipinski, B., Schill, J., and Holsboer, F. (2000) Reduced glutamate in the anterior cingulate cortex in depression: An in vivo proton magnetic resonance spectroscopy study, *Biol. Psychiatry 47*, 305-313.

13. Mangia, S., Tkac, I., Gruetter, R., Van de Moortele, P. F., Giove, F., Maraviglia, B., and Ugurbil, K. (2006) Sensitivity of single-voxel H-1-MRS in investigating the metabolism of the activated human visual cortex at 7 T, *Magn. Reson. Imaging 24*, 343-348.

14. Prichard, J., Rothman, D., Novotny, E., Petroff, O., Kuwabara, T., Avison, M., Howseman, A., Hanstock, C., and Shulman, R. (1991) Lactate rise detected by 1H NMR in human visual cortex during physiologic stimulation., *Proc. Natl. Acad. Sci. U. S. A. 88*, 5829-5831.

15. Govindaraju, V., Young, K., and Maudsley, A. A. (2000) Proton NMR chemical shifts and coupling constants for brain metabolites, *NMR in Biomedicine 13*, 129-153.

16. Stefan, D., Di Cesare, F., Andrasescu, A., Popa, E., Lazariev, A., Vescovo, E., Strbak, O., Williams, S., Starcuk, Z., Cabanas, M., van Ormondt, D., and Graveron-Demilly, D. (2009) Quantitation of magnetic resonance spectroscopy signals: the jMRUI software package, *Meas. Sci. Technol. 20*.

17. Smith, S. A., Levante, T. O., Meier, B. H., and Ernst, R. R. (1994) Computer Simulations in Magnetic Resonance. An Object-Oriented Programming Approach, *Journal of Magnetic Resonance, Series A 106*, 75-105.

18. Saunders De Fau - Howe, F. A., Howe Fa Fau - van den Boogaart, A., van den Boogaart A Fau - Griffiths, J. R., Griffiths Jr Fau - Brown, M. M., and Brown, M. M. Aging of the adult human brain: in vivo quantitation of metabolite content with proton magnetic resonance spectroscopy.

19. Provencher, S. W. (1993) Estimation of metabolite concentrations from localized in vivo proton NMR spectra, *Magnetic Resonance in Medicine 30*, 672-679.

20. Cramer, H. (1946) *Mathematical Methods of Statistics.*, University Press: Princeton, NS.

21. Rao, C. R. (1946) Minimum variance and the estimation of several parameters, *Proc. Cambridge Phil. Soc. 42*, 280-283.

22. Hancu, I. (2009) Optimized Glutamate Detection at 3T, *Journal of Magnetic Resonance Imaging 30*, 1155-1162.

23. Hancu, I. (2009) Which pulse sequence myo-inositol detection is optimal for at 3T?, *Nmr in Biomedicine 22*, 426-435.

24. Cavassila, S., Deval, S., Huegen, C., van Ormondt, D., and Graveron-Demilly, D. (2001) Cramer-Rao bounds: an evaluation tool for quantitation, *NMR in Biomedicine 14*, 278-283.

25. Cavassila, S., Deval, S., Huegen, C., van Ormondt, D., and Graveron-Demilly, D. (2000) Cramer-Rao Bound Expressions for Parametric Estimation of Overlapping Peaks: Influence of Prior Knowledge, *Journal of Magnetic Resonance 143*, 311-320.

26. Nguyen, H. M., Gahvari, Z. J., Haldar, J. P., Do, M. N., and Zhi-Pei, L. (2009) Cramer-Rao bound analysis of echo time selection for 1H-MR spectroscopy, In *Engineering in Medicine and Biology Society, 2009. EMBC 2009. Annual International Conference of the IEEE*, pp 2692-2695.

27. Smith, S. A., Levante, T. O., Meier, B. H., and Ernst, R. R. (1994) Computer Simulations in Magnetic Resonance. An Object Oriented Programming Approach, *J. Magn. Reson. 106a*, 75-105.

28. Bottomley, P. A. C. P., NY). (1984) Selective volume method for performing localized NMR spectroscopy, General Electric Company (Schenectady, NY), United States.

29. Rao, C. R. (1946) Minimum variance and the estimation of several parameters, *Proc. Cambridge Phil. Soc. 42*, 280-283.

30. Michaeli, S., Garwood, M., Zhu, X. H., DelaBarre, L., Andersen, P., Adriany, G., Merkle, H., Ugurbil, K., and Chen, W. (2002) Proton T2 relaxation study of water, N-acetylaspartate, and creatine in human brain using Hahn and Carr-Purcell spin echoes at 4T and 7T, *Magnetic Resonance in Medicine 47*, 629-633.

31. Snyder, J., and Wilman, A. (2010) Field strength dependence of PRESS timings for simultaneous detection of glutamate and glutamine from 1.5 to 7 T, *Journal of Magnetic Resonance 203*, 66-72.

32. Choi, C., Dimitrov, I. E., Douglas, D., Patel, A., Kaiser, L. G., Amezcua, C. A., and Maher, E. A. (2010) Improvement of resolution for brain coupled metabolites by optimized 1H MRS at 7 T, *NMR in Biomedicine 23*, 1044-1052.

33. Snyder, J., Thompson, R. B., and Wilman, A. H. (2010) Difference spectroscopy using PRESS asymmetry: application to glutamate, glutamine, and myo-inositol, *NMR in Biomedicine 23*, 41-47.

34. Hurd, R., Sailasuta, N., Srinivasan, R., Vigneron, D. B., Pelletier, D., and Nelson, S. J. (2004) Measurement of brain glutamate using TE-averaged PRESS at 3T, *Magnetic Resonance in Medicine 51*, 435-440.

35. Rowland, L. M., Kontson, K., West, J., Edden, R. A., Zhu, H., Wijtenburg, S. A., Holcomb, H. H., and Barker, P. B. (2012) In Vivo Measurements of Glutamate, GABA, and NAAG in Schizophrenia, *Schizophrenia Bulletin*.

36. Wassef A Fau - Baker, J., Baker J Fau - Kochan, L. D., and Kochan, L. D. GABA and schizophrenia: a review of basic science and clinical studies.

37. Stagg, C. J., Bachtiar, V., and Johansen-Berg, H. (2011) The Role of GABA in Human Motor Learning, *Curr. Biol. 21*, 480-484.

38. Benes, F. M., and Berretta, S. (2001) GABAergic interneurons: Implications for understanding schizophrenia and bipolar disorder, *Neuropsychopharmacology 25*, 1-27.

39. Henry, P. G., Dautry, C., Hantraye, P., and Bloch, G. (2001) Brain GABA editing without macromolecule contamination, *Magnetic Resonance in Medicine 45*, 517-520.

40. Terpstra, M., Ugurbil, K., and Gruetter, R. (2002) Direct in vivo measurement of human cerebral GABA concentration using MEGA-editing at 7 Tesla, *Magnetic Resonance in Medicine 47*, 1009-1012.

41. Near, J., Simpson, R., Cowen, P., and Jezzard, P. (2011) Efficient gamma-aminobutyric acid editing at 3T without macromolecule contamination: MEGA-SPECIAL, *NMR in Biomedicine 24*, 1277-1285.

42. Edden, R. A. E., and Barker, P. B. (2007) Spatial effects in the detection of γ-aminobutyric acid: Improved sensitivity at high fields using inner volume saturation, *Magnetic Resonance in Medicine 58*, 1276-1282.

43. Sokoloff, L. (1960) The metabolism of the central nervous system *in vivo*, In *Handbook of Physiology, Section I, Neurophysiology*, American Physiological Society, Washington, D.C.

44. Logothetis, N. K., Pauls, J., Augath, M., Trinath, T., and Oeltermann, A. (2001) Neurophysiological investigation of the basis of the fMRI signal, *Nature 412*, 150-157.

45. Baslow, M. H., and Guilfoyle, D. N. (2007) Using proton magnetic resonance imaging and spectroscopy to understand brain activation., *Brain and Language 102*, 153-164.

46. Gussew, A., Rzanny, R., Erdtel, M., Scholle, H. C., Kaiser, W. A., Mentzel, H. J., and Reichenbach, J. R. (2010) Time-resolved functional H-1 MR spectroscopic detection of glutamate concentration changes in the brain during acute heat pain stimulation, *Neuroimage 49*, 1895-1902.

47. Mangia, S., Giove, F., Tkac, I., Logothetis, N. K., Henry, P.-G., Olman, C. A., Maraviglia, B., Di Salle, F., and Ugurbil, K. (2008) Metabolic and hemodynamic events after changes in neuronal activity: current hypotheses, theoretical predictions and in vivo NMR experimental findings, *J Cereb Blood Flow Metab 29*, 441-463.

48. Mangia, S., Tkac, I., Gruetter, R., Van de Moortele, P. F., Maraviglia, B., and Ugurbil, K. (2007) Sustained neuronal activation raises oxidative metabolism to a new steady-state level: evidence from H-1 NMR spectroscopy in the human visual cortex, *J. Cereb. Blood Flow Metab. 27*, 1055-1063.

49. Pellerin, L., and Magistretti, P. J. (1994) Glutamate uptake into astrocytes stimulates aerobic glycolysis: a mechanism coupling neuronal activity to glucose utilization, *Proc. Natl. Acad. Sci. U. S. A. 91*, 10625-10629.

50. Rothman, D. L., Sibson, N. R., Hyder, F., Shen, J., Behar, K. L., and Shulman, R. G. (1999) In vivo nuclear magnetic resonance spectroscopy studies of the relationship between the glutamate-glutamine neurotransmitter cycle and functional neuroenergetics, *Philosophical Transactions of the Royal Society of London. Series B: Biological Sciences 354*, 1165-1177.

51. Zhu, X. H., and Chen, W. (2001) Observed BOLD effects on cerebral metabolite resonances in human visual cortex during visual stimulation: A functional H-1 MRS study at 4 T, *Magnetic Resonance in Medicine 46*, 841-847.

52. Schaller, B., Mekle, R., Xin, L., Kunz, N., and Gruetter, R. (2013) Net increase of lactate and glutamate concentration in activated human visual cortex detected with magnetic resonance spectroscopy at 7 tesla, *Journal of Neuroscience Research*, n/a-n/a.